# Setup of a carbon-cluster laser ion source and the application of the invariance theorem at ISOLTRAP

Diplomarbeit von

Christine Böhm

Institut für Physik
Johannes Gutenberg-Universität Mainz

CERN

# Setup of a carbon-cluster laser ion source and the application of the invariance theorem at ISOLTRAP

16. März 2009

# Contents

**1 Introduction** **1**

**2 Principle of Penning traps** **5**
- 2.1 Ideal Penning traps . . . . . 5
- 2.2 Real Penning traps . . . . . 8
  - 2.2.1 Electric field imperfections . . . . . 8
  - 2.2.2 Magnetic field imperfections . . . . . 8
  - 2.2.3 The invariance theorem . . . . . 9
- 2.3 Manipulation of ions in a Penning trap . . . . . 12
  - 2.3.1 Excitation of the ion motion . . . . . 12
  - 2.3.2 Buffer gas cooling . . . . . 14

**3 Experimental setup of ISOLTRAP** **17**
- 3.1 ISOLTRAP . . . . . 17
  - 3.1.1 The ISOLDE facility . . . . . 17
  - 3.1.2 Radiofrequency cooler and buncher . . . . . 20
  - 3.1.3 Preparation trap . . . . . 20
  - 3.1.4 Precision trap . . . . . 22
  - 3.1.5 Time-of-flight ion cyclotron resonance detection . . . . . 24
  - 3.1.6 Measurement timing sequence . . . . . 26
- 3.2 Mass determination . . . . . 26
  - 3.2.1 Measurement principle . . . . . 26
  - 3.2.2 Uncertainties in the mass determination . . . . . 27

**4 Beamtimes at ISOLTRAP in 2008** **29**

**5 Setup of a carbon-cluster laser ion source** **33**
- 5.1 Off-line ion sources at ISOLTRAP . . . . . 33
- 5.2 The ISOLTRAP carbon-cluster laser ion source . . . . . 33
  - 5.2.1 Improvements of the original source . . . . . 35
  - 5.2.2 Laser system . . . . . 36
  - 5.2.3 Ion optics . . . . . 38
  - 5.2.4 Carbon-cluster mass spectrum . . . . . 39

**6 Application of the invariance theorem 43**
  6.1 Measurements of the ion motional frequencies . . . . . . . . . . . . . . . . . . 43
  6.2 Experimental results and discussion . . . . . . . . . . . . . . . . . . . . . . . . 49
    6.2.1 Results and statistical uncertainties . . . . . . . . . . . . . . . . . . . 49
    6.2.2 Discussion of systematic uncertainties . . . . . . . . . . . . . . . . . . 51

**7 Conclusion and Outlook 59**

**Acknowledgements 69**

# List of Figures

1.1 Nuclide chart . . . 2

2.1 Typical Penning trap configurations . . . 6
2.2 Eigenmotions in a Penning trap . . . 7
2.3 Magnetic field in a real Penning trap . . . 9
2.4 Dipole and quadrupole excitation . . . 13
2.5 Magnetron radius as a function of the excitation time . . . 13
2.6 Conversion of a pure magnetron into a pure modified cyclotron motion . . . 14
2.7 Ion trajectories in a buffer gas-filled trap . . . 15

3.1 Photograph of the ISOLTRAP experiment . . . 18
3.2 Elements available as radioactive beams at ISOLDE . . . 18
3.3 Sketch of the experimental hall of the ISOLDE facility . . . 19
3.4 Sketch of the buncher . . . 20
3.5 The ISOLTRAP setup . . . 21
3.6 Preparation trap with main and correction electrodes . . . 22
3.7 Precision trap with main and correction electrodes . . . 23
3.8 Principle of the time-of-flight technique . . . 25
3.9 Cyclotron resonance curve of $^{12}\mathrm{C}_{10}^{+}$ . . . 25
3.10 Timing of the signals for the measurement procedure . . . 27

4.1 Cyclotron resonance curve of $^{128}\mathrm{Cd}^{+}$ . . . 31
4.2 Cyclotron resonance curve of $^{229}\mathrm{Rn}^{+}$ . . . 32

5.1 Off-line ion sources at ISOLTRAP . . . 34
5.2 Photograph of a Sigradur pellet . . . 34
5.3 Setup of the previous carbon-cluster laser ion source . . . 35
5.4 Photograph of the present carbon-cluster laser ion source . . . 36
5.5 Setup of the present carbon-cluster laser ion source . . . 37
5.6 Laser energy for different attenuation settings . . . 38
5.7 Spectrum of a Sigradur pellet . . . 40
5.8 Cooling resonance of $^{12}\mathrm{C}_{11}^{+}$ . . . 40
5.9 Cyclotron resonance curve of $^{12}\mathrm{C}_{11}^{+}$ . . . 41
5.10 Cyclotron resonance curve of $^{12}\mathrm{C}_{20}^{+}$ . . . 41

6.1 Excitation scheme for the determination of $\nu_c^{conv}$ . . . . . . . . . . . . . . . . 45
6.2 Excitation scheme for the determination of $\nu_+$ . . . . . . . . . . . . . . . . . . 46
6.3 Excitation scheme for the determination of $\nu_-$ . . . . . . . . . . . . . . . . . . 47
6.4 Excitation scheme for the determination of $\nu_z$ . . . . . . . . . . . . . . . . . . 48
6.5 Potential applied to the precision trap electrodes for the measurement of $\nu_z$ 49
6.6 Results for the frequency shift $\Delta\nu_c$ . . . . . . . . . . . . . . . . . . . . . . . 51
6.7 Deviations concerning the conversion and the axial frequency . . . . . . . . 52
6.8 Temperature changes versus time recorded close to the precision trap . . . . 54
6.9 Fluctuations of the voltages applied to the precision trap electrodes . . . . . 56

# List of Tables

1.1 Applications of mass measurements . . . . . . . . . . . . . . . . . . . . . . . . 1

2.1 Typical eigenfrequencies . . . . . . . . . . . . . . . . . . . . . . . . . . . . . . 8

3.1 Voltages applied to the electrodes of the precision trap. . . . . . . . . . . . . 23
3.2 Characteristics of the channeltron and the MCP detector . . . . . . . . . . . 24

4.1 Nuclides measured at ISOLTRAP in 2008 . . . . . . . . . . . . . . . . . . . . 30

5.1 Voltages applied to the electrodes of the carbon-cluster laser ion source . . 39

6.1 Results of the measurement concerning the invariance theorem . . . . . . . 50
6.2 Frequency shifts $\Delta\nu_c$ . . . . . . . . . . . . . . . . . . . . . . . . . . . . . 50
6.3 Deviations of the conversion and the axial frequency . . . . . . . . . . . . . 52
6.4 Excitation times and amplitudes . . . . . . . . . . . . . . . . . . . . . . . . . 57

# Chapter 1

# Introduction

The mass of an atom is a fundamental property and an important input parameter for many fields of science [Bla06]. Tab. 1.1 gives an overview of some fields of application. High-precision mass measurements are in general required to investigate atomic as well as nuclear binding energies represented by Einsteins famous equation $E = mc^2$. Since all interactions, i.e. the electromagnetic, the weak and the strong interaction, contribute to the binding energies, mass measurements allow tests of corresponding theories. Mass models [Gor08] and mass formulae can be tested by high-precision mass measurements as well as shell models and the appearance and disappearance of magic numbers [Thi75, Gue07] far away from the valley of stability. The knowledge of masses of short-lived nuclides has also an influence on the elaboration of stellar models, e.g. the rapid neutron (r-) and rapid-proton (rp-) capture process [Bar08]. Furthermore, a test of the unitarity of the Cabibbo-Kobayashi-Maskawa (CKM) quark-mixing matrix can be performed [Har08].

So far masses of more than 3200 nuclides are measured or extrapolated [Aud03] of which only about 300 are stable. For stable nuclides a relative mass precision down to $\delta m/m = 10^{-11}$ [Dyc04, Rai04, Red09] is achieved employing Penning traps as introduced in chapter 2 of this thesis, whereas short-lived nuclides are typically determined with a relative mass precision of $\delta m/m = 10^{-8}$ [Kel03], as illustrated by the color code in Fig. 1.1. With

| field of application | $\delta m/m$ |
|---|---|
| chemistry: identification of molecules | $10^{-5}$-$10^{-6}$ |
| nuclear physics: shells, sub-shells, pairing | $10^{-6}$ |
| nuclear fine structure: deformation, halos | $10^{-7}$-$10^{-8}$ |
| astrophysics: r-process, rp-process, waiting points | $10^{-7}$ |
| nuclear models and formulas: IMME | $10^{-7}$-$10^{-8}$ |
| weak interaction studies: CVC hypothesis, CKM unitarity | $10^{-8}$ |
| atomic physics: binding energies, QED | $10^{-9}$-$10^{-11}$ |
| metrology: fundamental constants, CPT | $\leq 10^{-10}$ |

**Table 1.1:** Mass measurements enter in a wide range of applications. Several fields and the corresponding required relative mass uncertainty $\delta m/m$ are listed.

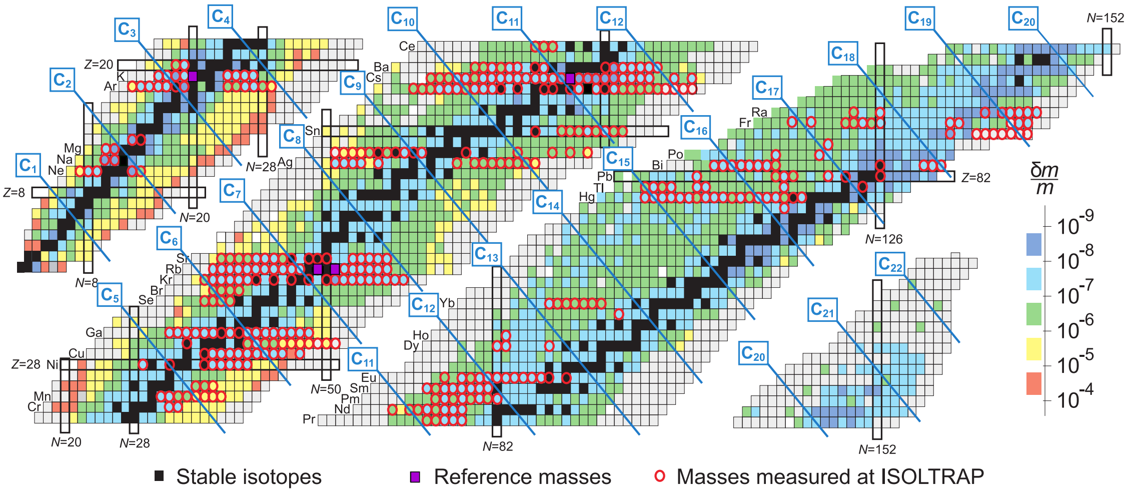

**Figure 1.1:** Nuclear chart with nuclides measured at ISOLTRAP (red circles), as well as the alkali reference ions (purple) and isobaric lines of carbon cluster ions [Bla05]. Further masses are shown with a color code indicating the relative precision of the mass data.

the triple trap mass spectrometer ISOLTRAP [Muk08], located at the online radioactive beam facility ISOLDE/CERN [Kug00], masses of more than 400 exotic nuclides have been determined until end of 2008. For some of them a mass uncertainty of $8{\cdot}10^{-9}$ has been achieved, which is presently the systematic uncertainty limit of ISOLTRAP [Kel03].
In general, the highest precision is reached for quantities, which are available by a frequency measurement. ISOLTRAP takes advantage of this fact by performing the mass determination via a measurement of the cyclotron frequency

$$\nu_c = \frac{q}{2\pi m}B,$$

of an ion with charge $q$ and mass $m$ in a magnetic field $B$ in a Penning trap system. At ISOLTRAP the precision in the determination of the cyclotron frequency is limited by the fluctuations of the magnetic field [Kel03]. Therefore, a magnetic field calibration using reference ions of a well-known mass is indispensable. In the context of this thesis an off-line ion source was installed at ISOLTRAP, which provides carbon cluster ions in a mass range covering a large fraction of the nuclear chart. Since there is a mass-dependent systematic uncertainty, which is increasing with the mass difference between the mass of the reference ion and the mass of the ion of interest $\Delta m = m_{ref} - m_{int}$, carbon cluster ions are minimizing this contribution to the total uncertainty. The mass difference is at maximum six atomic mass units, which is only one of the many advantages of this ion source [Bla02, Bla03b]. In addition carbon cluster ions are ideal reference ions since their mass is known exactly as the atomic mass unit is defined as one twelfth of the mass of the $^{12}$C atom [Emi95].

Chapter 2 of this thesis introduces the principles of Penning traps including a derivation of the invariance theorem [Bro82], which represents the connection between the cyclotron frequency of an ion stored in a pure magnetic field to the three independent motional eigenfrequencies of the ion in the electromagnetic field of a Penning trap. In chapter 3 an overview on the setup of the ISOLTRAP experiment as well as the measurement procedure and a detailed discussion of the sources of uncertainties will be given. Recent mass measurements in the year 2008 and their applications are summarized in chapter 4. The assembly of the carbon-cluster laser ion source and some specifications, which were measured in the context of this thesis, are reported in chapter 5. In chapter 6 the application of the invariance theorem will be depicted as well as corresponding results including a detailed description about sources of uncertainties. Finally, in chapter 7 a summary of the present thesis and an outlook to future measurements will be given.

Apart from technical developments at the carbon-cluster laser ion source and measurements concerning the invariance theorem several beamtimes were accomplished at ISOLTRAP in 2008. The aim of ISOLTRAP are high-precision mass measurements on short-lived exotic nuclides far away from stability. In 2008, a number of nuclides were successfully measured with mass uncertainties as low as $10^{-8}$, many of them studied for the first time: $^{126,128}$Cd, $^{136-146}$Xe, $^{194}$Hg, $^{194}$Au, $^{202}$Pb, $^{220}$Rn and $^{223-229}$Rn whereas $^{229}$Rn was the first isotope discovered in a Penning trap experiment.

# Chapter 2

# Principle of Penning traps

Penning traps allow three-dimensional trapping of charged particles by superimposing a weak hyperbolic electrical field with a strong homogeneous magnetic field. In the following ideal and real Penning traps are introduced. Ideal Penning traps are created by a harmonic potential and a perfectly aligned magnetic field while the electromagnetic field in a real Penning trap is disturbed by several imperfections.

## 2.1 Ideal Penning traps

Penning traps are used to store charged particles in three dimensions by electromagnetic fields. In 1989 Dehmelt was rewarded the Nobel Prize in physics [Deh90] for his studies with Penning trap experiments. These traps consist of a strong homogeneous magnetic field $\vec{B} = B\hat{e}_z$ and a weak electrostatic quadrupole field created by infinite hyperbolic electrodes. The harmonic trapping potential in the center of the trap is the result of applying voltages between the ring electrode and the endcaps. The axial confinement achieved by the electric field together with the radial confinement due to the Lorentz-force stores a particle with charge $q$. Ions in ideal Penning traps are located in a harmonic potential and the total force is given by:

$$\begin{aligned} \vec{F}_{\text{tot}} &= \vec{F}_{\text{Lorentz}} + \vec{F}_{\text{el}}, \\ &= q(\dot{\vec{r}} \times \vec{B}) + q\vec{E}(\vec{r}), \end{aligned} \tag{2.1}$$

with

$$\vec{F}_{\text{el}} = -q\vec{\nabla}U(\vec{r}), \tag{2.2}$$

where $U(\vec{r})$ is the potential:

$$U(\vec{r}) = U(r,z) = \frac{U_0}{2d^2}\left(z^2 - \frac{r^2}{2}\right),$$

with the trap geometry parameter $d^2 = \frac{1}{2}\left(z_0^2 + \frac{1}{2}r_0^2\right)$. The minimum distance from the center of the trap to the ring and the endcap electrodes is given by $r_0$ and $z_0$, respectively.

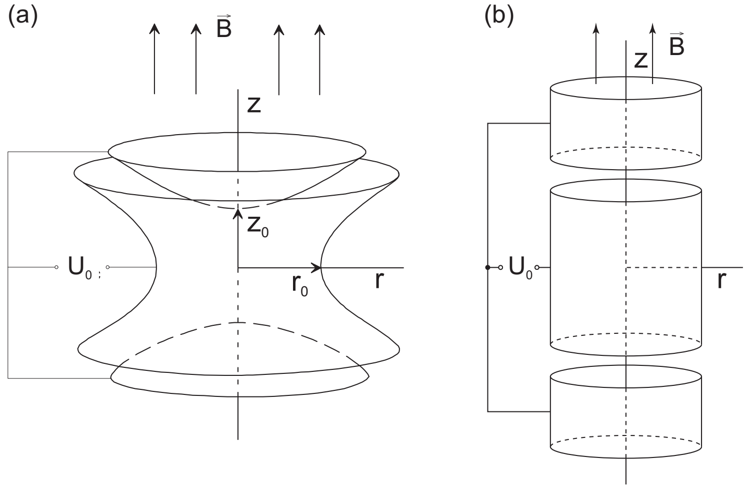

**Figure 2.1:** Sketch of Penning traps with conventional shapes. Applying a DC voltage between the endcaps and the ring electrode, both the a) hyperbolic as well as b) the cylindrical Penning trap, create a trapping potential in axial direction. The homogeneous magnetic field $\vec{B}$ defines the $z$-axis and confines the ions in radial direction.

Examples of two types of Penning traps with different electrode geometries are shown in Fig. 2.1.

Charged particles with mass $m$ perform in the magnetic field $B$ a circular motion with

$$\omega_c = \frac{q}{m}B, \tag{2.3}$$

which is called the cyclotron frequency. Due to $\vec{B} = B\hat{e}_z$ we can replace $B\hat{e}_z$ in Eq. (2.1) by Eq. (2.3) and plug in Eq. (2.2), which results in the equations of motion in radial and axial direction:

$$\ddot{x} = \dot{y}\omega_c + \frac{1}{2}\left(\frac{qU_0}{md^2}\right)x, \tag{2.4}$$

$$\ddot{y} = -\dot{x}\omega_c + \frac{1}{2}\left(\frac{qU_0}{md^2}\right)y, \tag{2.5}$$

$$\ddot{z} = -\left(\frac{qU_0}{md^2}\right)z. \tag{2.6}$$

The ion motion in axial direction is decoupled from the radial components and can be described as a harmonic oscillator. The coefficient in Eq. (2.6) is identified with the squared oscillation frequency:

$$\omega_z = \sqrt{\frac{qU_0}{md^2}}. \tag{2.7}$$

For the radial components the ansatz $u = x + iy$ together with the assumption $u = e^{-iwt}$ leads to:

$$\omega^2 - \omega_c \cdot \omega + \frac{1}{2}\omega_z^2 = 0. \tag{2.8}$$

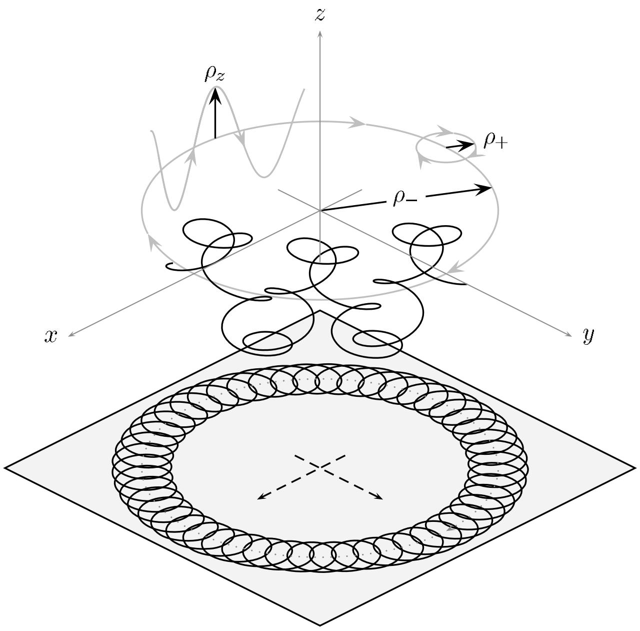

**Figure 2.2:** Ion motions in a Penning trap. $\rho_+$, $\rho_z$ and $\rho_-$ are the radii of the modified cyclotron, the axial and the magnetron motion, respectively. The black solid line (top) shows the superposition of all three eigenfrequencies, whereas the solid line below represents the superposition of the radial eigenfrequencies. The frequencies and amplitudes are not to scale.

The solution are the radial eigenfrequencies:

$$\omega_\pm = \frac{1}{2}\left(\omega_c \pm \sqrt{\omega_c^2 - 2\omega_z^2}\right). \tag{2.9}$$

To trap the ions the relation $\omega_c^2 > 2\omega_z^2$ must be fulfilled. Thus, we can derive the Taylor expansions for Eq. (2.9):

$$\omega_+ \approx \omega_c - \frac{U_0}{2d^2B}, \tag{2.10}$$

$$\omega_- \approx \frac{U_0}{2d^2B}, \tag{2.11}$$

which shows that the magnetron frequency $\omega_-$ is in first order mass independent. Ion trajectories for the modified cyclotron frequency $\omega_+$, the magnetron frequency $\omega_-$ and the axial frequency $\omega_z$ are shown in the example given in Fig. 2.2. All three eigenfrequencies obey the relations:

$$\omega_c = \omega_+ + \omega_-, \tag{2.12}$$

$$\omega_c^2 = \omega_+^2 + \omega_z^2 + \omega_-^2, \tag{2.13}$$

$$\omega_- < \omega_z < \omega_+, \tag{2.14}$$

$$\omega_z^2 = 2\omega_+\omega_-. \tag{2.15}$$

| | $A = 100$ | $A = 133$ |
|---|---|---|
| $\nu_+$ | 910 kHz | 682 kHz |
| $\nu_z$ | 44 kHz | 38 kHz |
| $\nu_-$ | 1.08 kHz | 1.08 kHz |

**Table 2.1:** Typical eigenfrequencies of two ion species with mass $m$=100 u and $m$=133 u respectively, in a hyperbolic Penning trap for the following parameters: $r_0$=13 mm, $z_0$=11.18 mm, $U_0$=8.4 V and $B$=5.9 T.

It is important to note that Eq. (2.12) is only true for ideal Penning traps while Eq. (2.13) is also true for real Penning traps with imperfections. Later the equation is called the invariance theorem, which will be discussed in more detail in Chap. (2.2.3). Typical frequencies for singly charged ions with mass 100 u and 133 u in a 5.9 T strong magnetic field in a potential depth of 8.4 V are given in Tab. 2.1.

## 2.2 Real Penning traps

The electromagnetic field in a real Penning trap deviates from the ideal case due to trap imperfections and field inhomogeneities [Bro86]. This leads to shifts in eigenfrequencies (see Chap. (2.2.3)). Several imperfections are discussed below.

### 2.2.1 Electric field imperfections

The ring electrodes are segmented in order to allow the manipulation of the ion motion (see Chap. (2.3)). In addition to this, the boreholes in the endcaps for ion in- and ejection are responsible for the distortion of the electric field. Further field imperfections due to finite, not perfectly fabricated electrodes result in a potential, which is approximately harmonic in the center of the Penning trap only. Another reason for the perturbation of the potential is given by the alignment of the electrodes. In order to compensate for these imperfections correction electrodes have to be installed.

### 2.2.2 Magnetic field imperfections

Magnetic field imperfections due to the misalignment of the magnetic field axis with respect to the symmetry axis of the Penning trap as well as changes in the amplitude of the magnetic field of the superconducting magnets influence the frequencies. Another problem is caused by the magnetization of materials used as trap components or being in the surrounding, which cause inhomogeneities of the magnetic field. The magnetization influences the shape of the field proportional to the magnetic susceptibility of the materials.

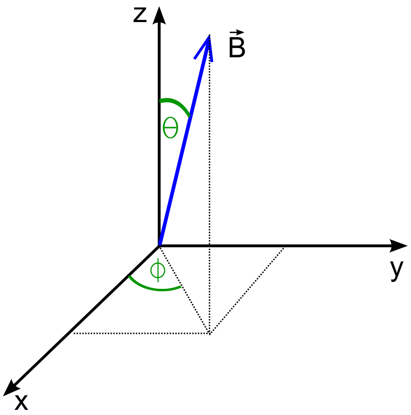

**Figure 2.3:** The magnetic field in an ideal Penning trap defines the $z$-axis. In a real Penning trap it is tilted by an angle $\theta$. Assuming cylindric symmetry $\phi$ can be set to zero.

### 2.2.3 The invariance theorem

In 1982 Brown and Gabrielse [Bro82] described the invariance theorem Eq. (2.13), which shows the relation between the eigenfrequencies of an ion in a Penning trap and the cyclotron frequency[1]. The ion motions in a trap are influenced by unavoidable imperfections but the invariance theorem states the possibility of measuring the cyclotron frequency very precisely independent of the perturbations in first order, which will be derived in the following. The deformation of the electromagnetic field can be described by two parameters. The ellipticity $\epsilon$ with $\epsilon = 0$ for ideal Penning traps contains the distortion of the electrical field whereas the angles for the magnetic field with respect to the symmetry axis of the trap are given by $\theta$ and $\phi$, as shown in Fig. 2.3 where $\phi$ can be set to zero since we assume a system with cylindrical symmetry. In order to show how the ellipticity $\epsilon$ and the angle $\theta$ influence the cyclotron frequency the derivative of the invariance theorem in terms of these two parameters will be given below.

The motion of a particle in a real Penning trap is influenced by the Lorentz-force including a misaligned magnetic field $\vec{B}_{\text{tilt}}$ and the electrical force including a potential with perturbation $U_{\text{perturb}}$:

$$\vec{F}_{\text{tot}} = q(\dot{\vec{r}} \times \vec{B}_{\text{tilt}}) - q(\vec{\nabla} U_{\text{perturb}}). \tag{2.16}$$

In contrast to the ideal case the potential energy of an ion in a real Penning trap contains a perturbation term:

$$U_{\text{perturb}} = \frac{1}{2} m \omega_z^2 (z^2 - \frac{1}{2}(x^2 + y^2) - \underbrace{\frac{1}{2}\epsilon(x^2 - y^2)}_{\text{perturbation}}\,). \tag{2.17}$$

Higher order perturbations are neglected due to little influence. The magnetic perturbation field $\vec{B}_{\text{tilt}}$ is considered to be not necessarily parallel to the symmetry axis of the trap, therefore it is

---

[1] Cyclotron frequency in absence of an electrical field.

$$\begin{aligned} B_x &= B\sin(\theta)\cos(\phi), \\ B_y &= B\sin(\theta)\sin(\phi), \\ B_z &= B\cos(\theta), \end{aligned}$$

with $\theta = \phi = 0$ in a perfect aligned Penning trap. Hence we can derive the following equations of motion:

$$\begin{aligned} \ddot{x} &= \dot{y}\,\omega_c\cos(\theta) - \dot{z}\,\omega_c\sin(\theta)\sin(\phi) + \frac{1}{2}\omega_z^2 x(1+\epsilon), \\ \ddot{y} &= \dot{z}\,\omega_c\sin(\theta)\cos(\phi) - \dot{x}\,\omega_c\cos(\theta) + \frac{1}{2}\omega_z^2 y(1-\epsilon), \\ \ddot{z} &= \dot{x}\,\omega_c\sin(\theta)\sin(\phi) - \dot{y}\,\omega_c\sin(\theta)\cos(\phi) - \omega_z^2. \end{aligned}$$

Using the ansatz $u = e^{-i\omega t}$ with $u = \{x, y, z\}$ the system of differential equations can be written as a determinant:

$$F(\omega) = \det\begin{vmatrix} \omega^2 + \frac{1}{2}(1+\epsilon)\omega_z^2 & -i\omega\omega_c\cos(\theta) & i\omega\omega_c\sin(\theta)\sin(\phi) \\ i\omega\omega_c\cos(\theta) & \omega^2 + \frac{1}{2}(1-\epsilon)\omega_z^2 & -i\omega\omega_c\cos(\phi)\sin(\theta) \\ -i\omega\omega_c\sin(\theta)\sin(\phi) & i\omega\omega_c\cos(\phi)\sin(\theta) & \omega^2\ \omega_z^2 \end{vmatrix}.$$

Calculating the determinant we obtain:

$$\begin{aligned} F(\omega) &= \omega^6 + \omega^4\left(-\omega_c^2\cos^2(\theta) - \omega_c^2\cos^2(\phi)\sin^2(\theta) - \omega_c^2\sin^2(\phi)\sin^2(\theta)\right) \\ &\quad + \omega^2\Bigg[\frac{1}{2}\Bigg(-\frac{3}{2}\omega_z^4 - \frac{1}{2}\omega_z^2\epsilon^2 + 2\omega_c^2\cos^2(\theta) - \omega_c^2\omega_z^2\cos^2(\phi)\sin^2(\theta) \\ &\quad - \epsilon\,\omega_c^2\omega_z^2\cos^2(\phi)\sin^2(\theta) - \omega_c^2\omega_z^2\sin^2(\phi)\sin^2(\theta) \\ &\quad + \epsilon\,\omega_c^2\omega_z^2\sin^2(\phi)\sin^2(\theta)\Bigg)\Bigg] - \frac{1}{4}\omega_z^6\left(1-\epsilon^2\right). \end{aligned} \tag{2.18}$$

Since the eigenfrequencies are known, it is possible to provide the characteristic polynomial [Bro86]:

$$\begin{aligned} F(\omega) &= (\omega^2 - \bar{\omega}_+^2)(\omega^2 - \bar{\omega}_z^2)(\omega^2 - \bar{\omega}_-^2) \\ &= \omega^6 - \omega^4\underbrace{(\bar{\omega}_+^2 + \bar{\omega}_-^2 + \bar{\omega}_z^2)}_{\text{Part C}} + \omega^2\underbrace{(\bar{\omega}_+^2\bar{\omega}_-^2 + \bar{\omega}_+^2\bar{\omega}_z^2 + \bar{\omega}_-^2\bar{\omega}_z^2)}_{\text{Part A}} - \underbrace{\bar{\omega}_+^2\bar{\omega}_z^2\bar{\omega}_-^2}_{\text{Part B}}. \end{aligned}$$

All frequencies labeled with a bar $\bar{\omega}$ correspond to eigenfrequencies measured in a real Penning trap ($\bar{\omega} = \omega(\epsilon, \theta, \phi)$).
Arranging the terms of the characteristic polynomial in powers of $\omega^n$ leads to three equations, which are obtained by comparing the coefficients in Eq. (2.18) with part A, B and C. In the following these parts will be discussed separately:

### Part A

By comparing the coefficients of $\omega^2$ we obtain:

$$\begin{aligned}\bar{\omega}_+^2\bar{\omega}_z^2+\bar{\omega}_+^2\bar{\omega}_-^2+\bar{\omega}_z^2\bar{\omega}_-^2 = \omega_c^2\omega_z^2\left(1-\frac{3}{2}\sin^2(\theta)-\frac{\epsilon}{2}\sin^2(\phi)\cos(2\phi)\right)\\ -\frac{3}{4}\omega_z^4\left(1+\frac{1}{3}\epsilon^2\right).\end{aligned}$$

Deviding by $\bar{\omega}_+^4$ leads to terms in the order of $10^{-6}$ and $10^{-9}$, which will be neglected. This approximation is feasible since these terms would not influence the final result. Rearranging the remaining terms leads to:

$$\bar{\omega}_z^2 \approx \omega_z^2\left[1-\frac{3}{2}\sin^2(\theta)\left(1+\frac{1}{3}\epsilon\cos(2\phi)\right)\right]. \tag{2.19}$$

This result will be taken into account in part B.

### Part B

The second equation, which is obtained by the comparison of the characteristic polynomial with Eq. (2.18)

$$\bar{\omega}_+^2\bar{\omega}_z^2\bar{\omega}_-^2 = \frac{1}{4}\bar{\omega}_z^6\left(1-\epsilon^2\right), \tag{2.20}$$

can be written as

$$\begin{aligned}\bar{\omega}_- &\approx \tilde{\omega}_-\sqrt{1-\epsilon^2}\left[1-\frac{3}{2}\sin^2(\theta)(1+\frac{1}{3}\epsilon\cos(2\phi))\right]^{-3/2}\\ &\approx \tilde{\omega}_-\left(1+\frac{9}{4}\theta^2-\frac{1}{2}\epsilon^2\right),\end{aligned} \tag{2.21}$$

by using Eq. (2.19) as well as a Taylor expansion.

### Part C

Finally, the comparison leads also to the invariance theorem:

$$\omega_c^2 = \bar{\omega}_+^2+\bar{\omega}_z^2+\bar{\omega}_-^2. \tag{2.22}$$

Introducing $\tilde{\omega}_- = \frac{\bar{\omega}_z^2}{2\bar{\omega}_+}$ Eq. (2.22) can be rearranged to:

$$\begin{aligned}\frac{\omega_c}{\bar{\omega}_+} &= \frac{1}{\bar{\omega}_+}\sqrt{(\bar{\omega}_++\tilde{\omega}_-)^2-(\tilde{\omega}_-^2-\bar{\omega}_-^2)}\\ &= \sqrt{1+\left(\frac{2\cdot\tilde{\omega}_-}{\bar{\omega}_z}\right)^2+\left(\frac{\bar{\omega}_-}{2\cdot\tilde{\omega}_-}\right)^2\left[\left(\frac{2\cdot\tilde{\omega}_-}{\bar{\omega}_z}\right)^2\right]^2}.\end{aligned} \tag{2.23}$$

The Taylor expansion of Eq. (2.23) for small values of $\left(\frac{2\tilde{\omega}_-}{\bar{\omega}_z}\right)^2$ is given by[2]:

$$\frac{\omega_c}{\bar{\omega}_+} \approx 1 + \frac{1}{2}\left(\frac{\bar{\omega}_z}{\bar{\omega}_+}\right)^2 + \frac{1}{8}\left(\frac{\bar{\omega}_z}{\bar{\omega}_+}\right)^4 \left[\left(\frac{\bar{\omega}_-}{\tilde{\omega}_-}\right)^2 - 1\right]. \tag{2.24}$$

Using Eq. (2.21) and Eq. (2.19) we obtain for Eq. (2.24):

$$\frac{\omega_c}{\bar{\omega}_+} \approx 1 + \frac{1}{2}\left(\frac{\bar{\omega}_z}{\bar{\omega}_+}\right)^2 + \frac{9}{16}\left(\frac{\bar{\omega}_z}{\bar{\omega}_+}\right)^4 \left(\theta^2 - \frac{2}{9}\epsilon^2\right). \tag{2.25}$$

The neglect of the third term in Eq. (2.25) in combination with Eq. (2.21) allows the calculation of the mass-independent frequency shift:

$$\begin{aligned} \Delta\bar{\omega}_c &= \bar{\omega}_c - \omega_c, \\ \Delta\bar{\omega}_c &\approx \bar{\omega}_- \left(\frac{9}{4}\theta^2 - \frac{1}{2}\epsilon^2\right). \end{aligned} \tag{2.26}$$

Eq. (2.26) shows that the determination of the ellipticity $\epsilon$ and the tilting angle $\theta$ of the magnetic field provide the input parameters for the calculation of the frequency shift. Correcting for this systematic effect one can decrease the uncertainty in the determination of the cyclotron frequency.

## 2.3 Manipulation of ions in a Penning trap

### 2.3.1 Excitation of the ion motion

**Dipole excitation**

A dipole excitation addresses single eigenmotions in a Penning trap. When a dipole excitation with $\omega_{\mathrm{rf}} = \omega_+$ is applied to two opposite ring segments (as shown in Fig. 2.4a) the radius for the modified cyclotron motion increases. The effect on the magnetron motion for $\omega_{\mathrm{rf}} = \omega_-$ is shown in Fig. 2.5 [Bla03a]. The magnetron radius depends on the duration of the excitation time $\mathrm{T}_d$ but also on the initial phase difference between the ion motion and the rf frequency. The axial motion can be influenced as well by applying a dipole excitation, here to the endcaps. This leads to a higher axial amplitude and will be further discussed in Chap. (6.1). The dipolar driving field can be written as:

$$\vec{E}_x = \frac{U_0}{a}\cos(\omega_{\mathrm{rf}}t - \phi_{\mathrm{rf}})\hat{x} \tag{2.27}$$

where $U_0$ is the rf voltage amplitude at a distance $a$ from the trapping center. This kind of excitation can be used to determine individual eigenfrequencies by resonant excitation (see Chap. (6)) or to remove unwanted contaminations from the trap.

---

[2] The general Taylor expansion of a root function $\sqrt{f(x)} = \sqrt{1 + x + \left(\frac{2\cdot\tilde{\omega}_-}{\bar{\omega}_z}\right)^2 \cdot x^2}$ can be written as $\sqrt{f(x)} = \sqrt{f(a)} + \frac{f'(a)(x-a)}{2\sqrt{f(a)}} + \left(\frac{f''(a)}{4\sqrt{f(a)}} + \frac{f'(a)^2}{8f(a)^{\frac{2}{3}}}\right)(x-a)^2 + O(x^3)$.

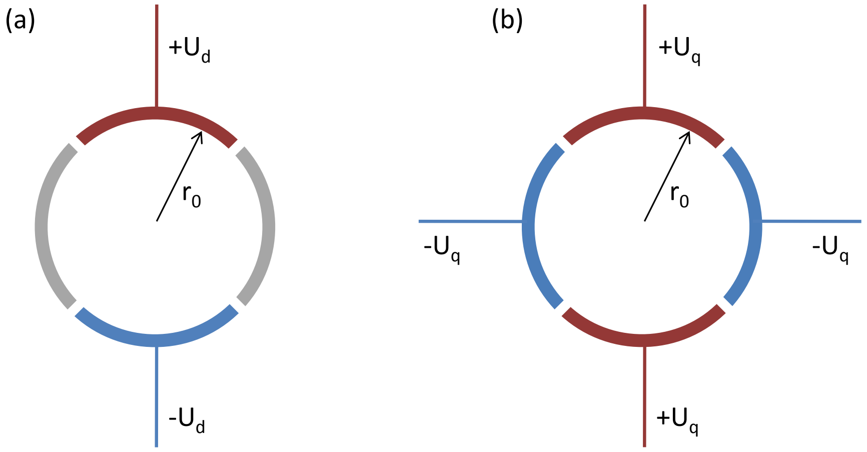

**Figure 2.4:** For a dipolar excitation voltages with 180° phase-shift are applied to two diametral electrodes (a) while a quadrupolar excitation requires an rf voltage at all electrodes (b). The dipole excitation addresses single eigenmotions while the quadrupolar excitation with an adequate frequency transfers the energy of one eigenmotion into another.

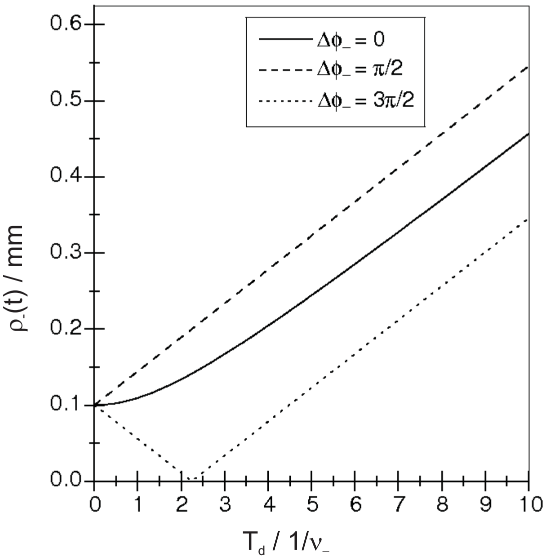

**Figure 2.5:** The magnetron radius of a stored ion as a function of the duration of the dipolar excitation $T_d$ for three different phase differences $\Delta\Phi_-$ between the ion motion and the rf signal [Bla03a]. Only in the case of $\Delta\Phi_- = 3/2\pi$ the increase in the magnetron radius starts continuously from beginning on.

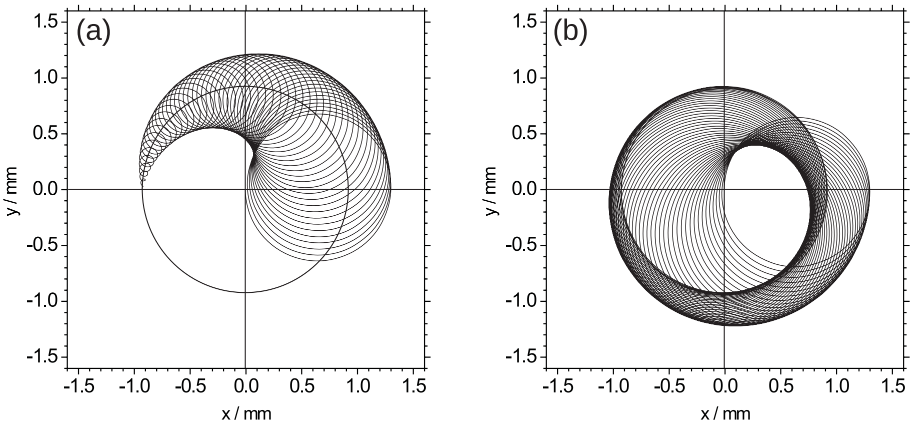

**Figure 2.6:** The conversion of a pure magnetron into a pure modified cyclotron motion is performed by applying a quadrupole excitation with $\omega_{\mathrm{rf}} = \omega_+ + \omega_-$. a) shows the ion trajectories for the first half and b) for the second half of the conversion. The circle in a) with a radius $r \approx 0.9$ mm indicates the initial magnetron radius.

### Quadrupole excitation

A quadrupole excitation is realized by applying 180° phase-shifted voltages to opposite segments of the four-fold segmented ring electrodes, as shown in Fig. 2.4b. The electrical field is given by:

$$\vec{E}_x = \frac{2U_0}{r_0^2}\cos(\omega_{\mathrm{rf}}t - \phi_{\mathrm{rf}})y\hat{e}_x \tag{2.28}$$

and

$$\vec{E}_y = \frac{2U_0}{r_0^2}\cos(\omega_{\mathrm{rf}}t - \phi_{\mathrm{rf}})x\hat{e}_y. \tag{2.29}$$

In contrast to a dipolar excitation, two eigenmotions are addressed simultaneously. An azimuthal quadrupole field with $\omega_{\mathrm{rf}} = \omega_+ + \omega_-$ couples the slow magnetron motion with the fast modified cyclotron motion resulting in an energy transfer from one to the other eigenmotion (see Fig. 2.6). The time needed for one complete conversion depends amongst others on the amplitude of the rf voltage $U_0$ and the magnetic field $B$:

$$T_d = \pi\frac{m}{q}\frac{a^2}{2U_0}(\omega_+ + \omega_-) \approx \pi\frac{a^2}{2qU_0}B. \tag{2.30}$$

Applying the excitation with $\omega_{\mathrm{rf}} = \omega_+ + \omega_-$ for a longer time means that the magnetron motion and the modified cyclotron motion are periodically converted into each other [Kön95a].

## 2.3.2 Buffer gas cooling

Buffer gas cooling is a technique which is often used in trap experiments to decrease the phase-space distribution of the ion cloud in order to simplify the ion cloud transport. In combination with a quadrupole excitation it allows also for isobaric purification, as

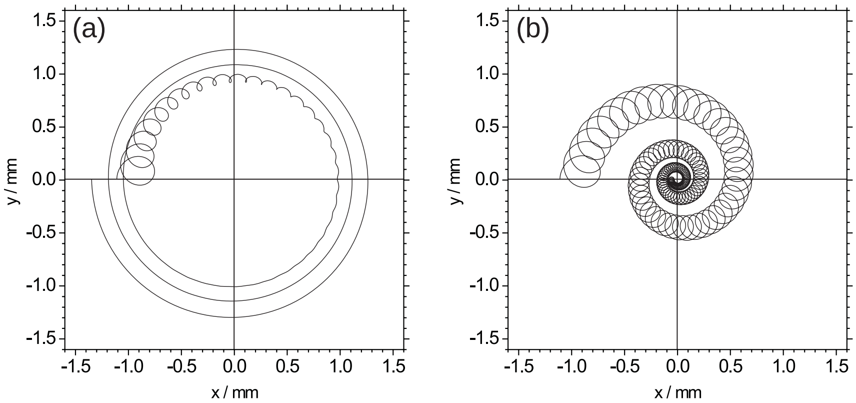

**Figure 2.7:** Calculated ion trajectories in a buffer gas filled trap. The buffer gas causes a velocity dependent damping force which lowers the cyclotron radius while the magnetron radius is increasing (a). Part (b) shows the effect of an additional applied azimuthal quadrupole excitation, which is responsible for centering due to the coupling of $\omega_+$ and $\omega_-$. Since $\omega_+$ is mass dependent the combination of buffer gas cooling and an azimuthal quadrupole excitation is mass selective.

demonstrated in Fig. 2.7. In order to minimize the emittance of an ion beam a damping force is required corresponding to Liouville´s theorem. In buffer gas filled traps ions are loosing their energy due to inelastic scattering processes with the lighter buffer gas atoms. Nobel gases are typically used as buffer gas atoms since the risk of charge exchange processes is very low due to their high ionization potential. If the ions are much heavier than the buffer gas atoms a thermal equilibrium is reached in about 1 ms [Her01]. The damping force $\vec{F}$ depends on the velocity $\vec{v}$ of the ions with mass $m$:

$$\vec{F} = -\delta m \vec{v}, \tag{2.31}$$

with the damping parameter:

$$\delta = \frac{q}{m} \frac{1}{\mu_{ion}} \frac{T_N}{T} \frac{p}{p_N}, \tag{2.32}$$

where $\frac{T}{T_N}$ and $\frac{p}{p_N}$ are temperature and pressure in fractions of the normal temperature and pressure, respectively. The reduced ion mobility $\mu_{ion}$ is assumed to be constant for low energies for a certain species of ions and buffer gas atoms.

# Chapter 3

# Experimental setup of ISOLTRAP and measurement procedure

## 3.1 ISOLTRAP

The ISOLTRAP (Isotope Separator On-Line TRAP) experiment [Muk08] located at the ISOLDE facility [Kug00] is a triple trap mass spectrometer dedicated to high-precision mass measurements of exotic, short-lived nuclides. Over 400 masses with half-lives down to 65 ms [Kel04] have been investigated with a relative mass uncertainty down to $\delta m/m = 8 \cdot 10^{-9}$ [Kel03]. The setup consists of three functional parts, which are highlighted in Fig. 3.1: The high energetic quasi-continuous ion beam coming from ISOLDE is first stopped in a linear radiofrequency quadrupole ion trap [Her01] held at high voltage, where the ions are stopped, cooled and bunched for the delivery and injection in the tandem Penning trap system. In the preparation trap buffer gas cooling in combination with an azimuthal quadrupole excitation is applied [Sav91] so that an isobarically pure ion bunch can be injected into the precision trap, which is dedicated for mass measurements using the time-of-flight ion cyclotron resonance detection technique. In the following a detailed description of the ISOLDE facility and the ISOLTRAP experiment will be given.

### 3.1.1 The ISOLDE facility

The ISOLDE facility [Kug00] is an isotope on-line mass separator at the European Organisation for Nuclear Research (CERN, Geneva, Switzerland), which is devoted to the production of exotic, short-lived nuclides. These radionuclides are created in nuclear reactions (spallation, fragmentation or fission) induced by 1 or 1.4-GeV protons impinging on a thick target, e.g. uranium carbide $UC_x$. Being accelerated in the Proton Synchrotron Booster (PSB) the protons come in bunches of up to 2.1 $\mu$A intensity, i.e. up to $3.2 \cdot 10^{13}$ protons per pulse every 1.2 s or its multiples, whereas in maximum only one half of the pulses is directed to the ISOLDE targets.

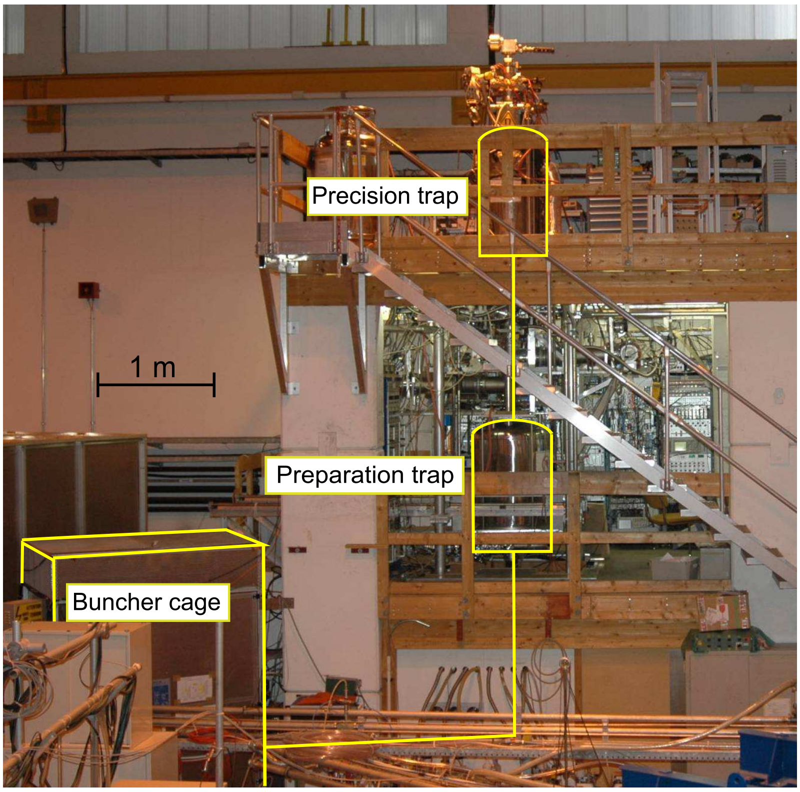
Precision trap
1 m
Preparation trap
Buncher cage

**Figure 3.1:** Photograph of the ISOLTRAP experiment with the three ion traps dedicated to preparation, purification and mass determination of radioactive ions [Muk08]. For more details see text.

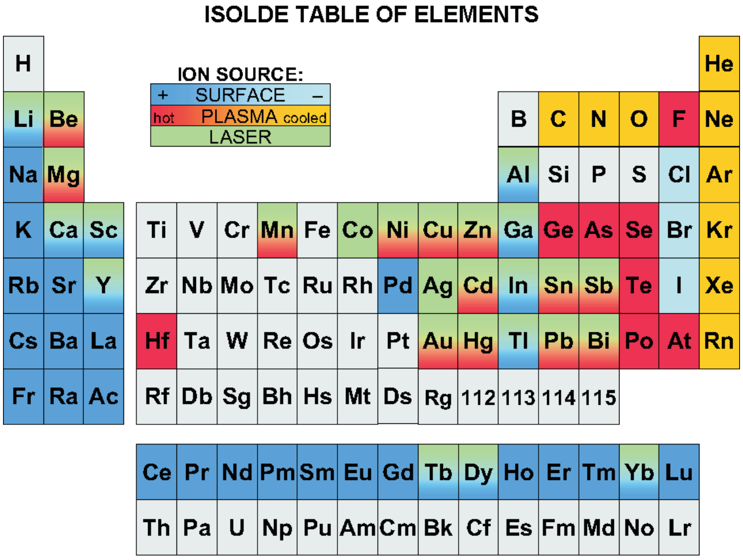
ISOLDE TABLE OF ELEMENTS
ION SOURCE:
+ SURFACE –
hot PLASMA cooled
LASER

| | | | | | | | | | | | | | | | | | |
|---|---|---|---|---|---|---|---|---|---|---|---|---|---|---|---|---|---|
| H | | | | | | | | | | | | | | | | | He |
| Li | Be | | | | | | | | | | | B | C | N | O | F | Ne |
| Na | Mg | | | | | | | | | | | Al | Si | P | S | Cl | Ar |
| K | Ca | Sc | Ti | V | Cr | Mn | Fe | Co | Ni | Cu | Zn | Ga | Ge | As | Se | Br | Kr |
| Rb | Sr | Y | Zr | Nb | Mo | Tc | Ru | Rh | Pd | Ag | Cd | In | Sn | Sb | Te | I | Xe |
| Cs | Ba | La | Hf | Ta | W | Re | Os | Ir | Pt | Au | Hg | Tl | Pb | Bi | Po | At | Rn |
| Fr | Ra | Ac | Rf | Db | Sg | Bh | Hs | Mt | Ds | Rg | 112 | 113 | 114 | 115 | | | |
| | | | Ce | Pr | Nd | Pm | Sm | Eu | Gd | Tb | Dy | Ho | Er | Tm | Yb | Lu | |
| | | | Th | Pa | U | Np | Pu | Am | Cm | Bk | Cf | Es | Fm | Md | No | Lr | |

**Figure 3.2:** Periodic table of elements which are available as radioactive beams at ISOLDE. The colors indicate the ionization process applied. (Courtesy of Luis Fraile.)

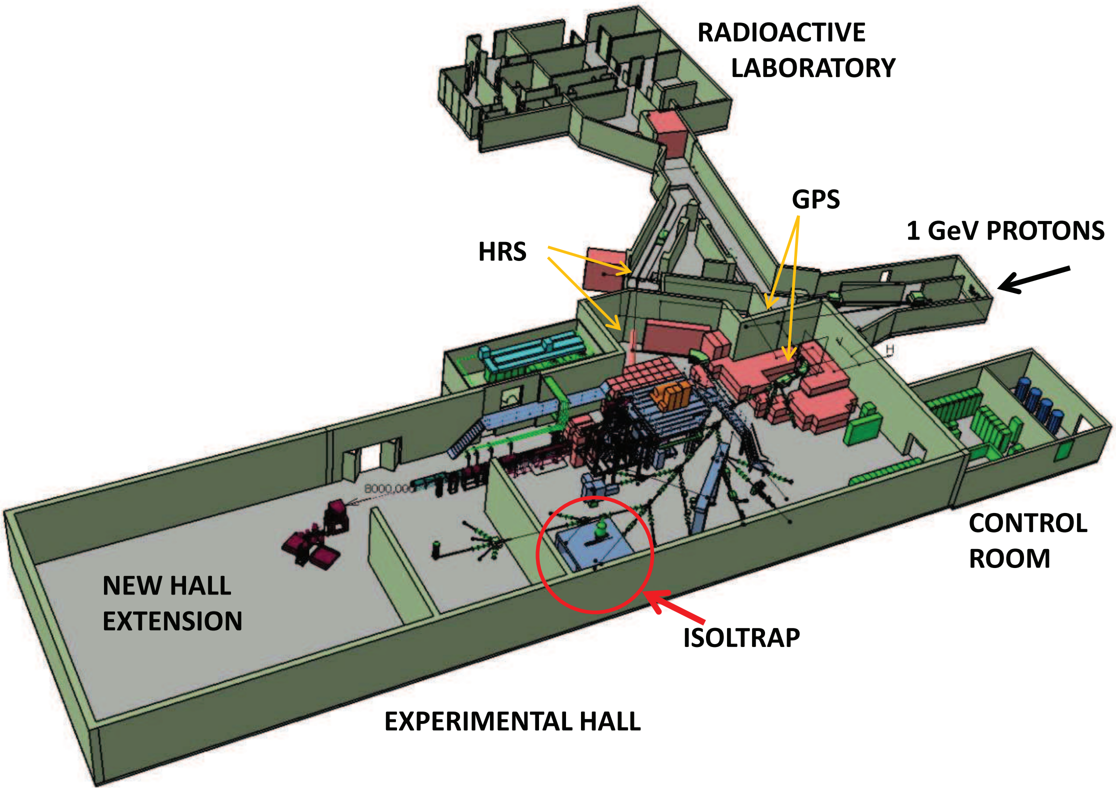

**Figure 3.3:** Experimental hall of the ISOLDE facility [Kug00]. On the upper right the protons coming from the Proton Synchrotron Booster enter the hall and are impinged on a thick target, typically $UC_x$ or $ThC_x$, to create radioactive nuclides. Two target stations, GPS or HRS, are available. After extraction and ionization the radionuclides are mass separated by one of the mass filters and pass ion optics before they enter ISOLTRAP via the central beamline.

The reaction products are ionized either by surface ionization, resonant laser ionization (RILIS) or plasma ionization [Kös03]. Fig. 3.2 shows the chemical elements, which are available as radioactive beams at ISOLDE. Refractory elements are not available due to their long release times. Being accelerated to 30 - 60 keV the ions are finally separated by one of the two magnetic mass filters, the General Purpose Separator (GPS, mass resolution $m/\Delta m \approx 1000$) or the High Resolution Separator (HRS, mass resolution $m/\Delta m \approx 5000$, [ISO03]). The radioactive ion beam is then distributed to different experiments situated at ISOLDE (see Fig. 3.3), whereas the central beamline transports the ions to ISOLTRAP.

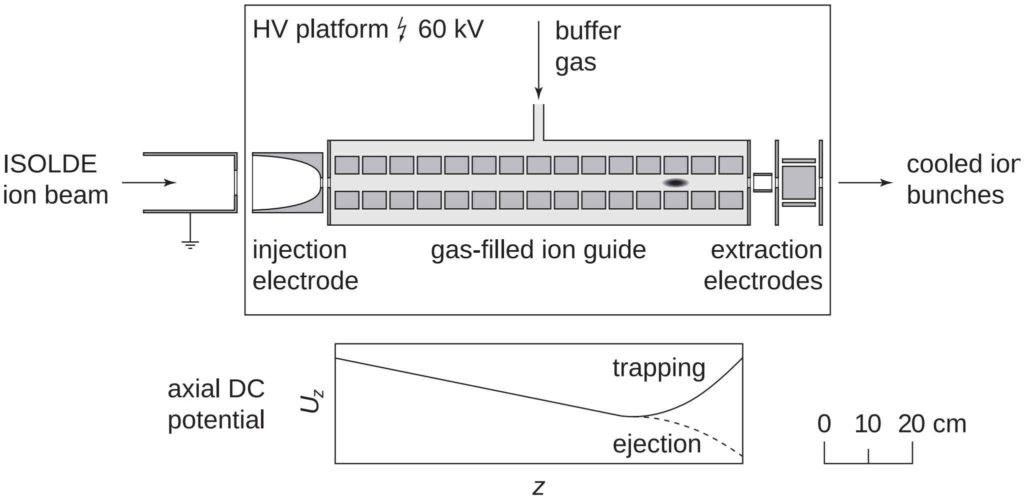

**Figure 3.4:** In the buncher the ions, coming from ISOLDE as a quasi-continuous ion beam with an energy of up to 60 keV, are accumulated and cooled by buffer-gas collisions. The linear Paul trap confines the ions in radial direction by applying an rf voltage to the four rods, whereas the segmentation of the rods allows to apply a DC voltage so that there is also an axial confinement. Afterwards the ions are ejected in bunches of about 1 $\mu$s length and pulsed down to an energy of 2.5 keV in the pulsed drift tube.

### 3.1.2 Radiofrequency cooler and buncher

The linear radiofrequency quadrupole cooler and buncher [Her01] is the first ISOLTRAP trap, where the continuous beam coming from ISOLDE is stopped after being electrostatically retarded by the injection electrode. The ions are trapped in the linear Paul trap, which consists of four rods where an rf voltage is applied to achieve a radial trapping potential. In order to apply an axial trapping potential the rods have to be segmented as shown in Fig. 3.4. The buncher is filled with helium to perform buffer gas cooling resulting in a damped ion motion. This leads together with the radial trapping potential and the axial confinement to an accumulation of the ions in the potential minimum of the buncher (see lower part of Fig. 3.4). After some ms they are ejected as a bunch with a length of about 1 $\mu$s towards the preparation trap. Behind the buncher a pulsed drift tube decreases the potential of the ion bunches so that their remaining kinetic transport energy is about 2.5 keV, allowing for an efficient 90° bending to the vertical beamline, see Fig. 3.5.

### 3.1.3 Preparation trap

The cylindrical Penning trap [Bec93] consists of an eight-fold segmented ring electrode, four-fold segmented endcaps and four-fold segmented correction electrodes, as shown in Fig. 3.6. The large inner radius ($r_i$=17.5 mm) allows to accept a quite large ion bunch. A homogeneous magnetic field of $B$ = 4.7 T is provided by a superconducting magnet surrounding the preparation trap. The trap is filled with helium gas at a pressure of about $10^{-4}$ mbar to cool the axial and radial ion motions by buffer gas collisions. A dipolar

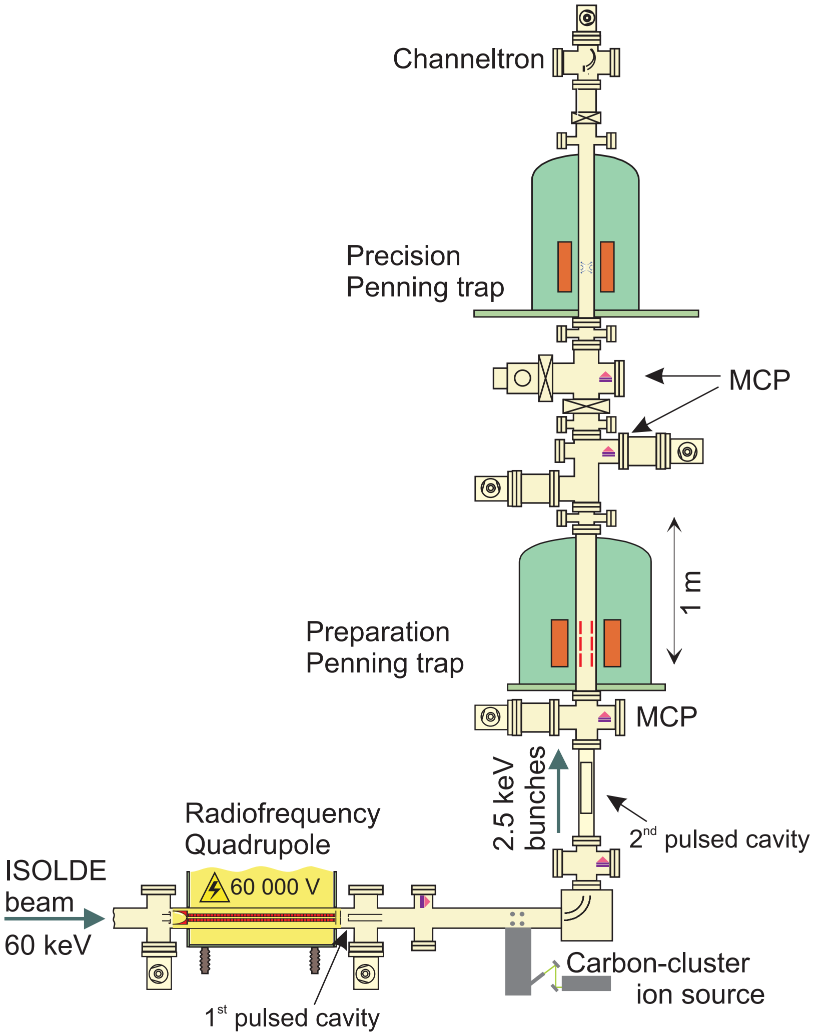
Channeltron
Precision
Penning trap
MCP
1 m
Preparation
Penning trap
MCP
2.5 keV
bunches
2nd pulsed cavity
Radiofrequency
Quadrupole
60 000 V
ISOLDE
beam
60 keV
1st pulsed cavity
Carbon-cluster
ion source

**Figure 3.5:** The short-lived radionuclides reach the buncher with a kinetic energy of up to 60 keV where they are accumulated, cooled and bunched. After ejection the potential energy is lowered in a pulsed drift tube down to about 2.5 keV. After a second deceleration step the ion cloud is injected into the preparation trap where contaminants are removed by a mass selective buffer gas cooling technique. Finally, they are fed into the upper trap for precision mass measurements via the determination of the cyclotron frequency employing the time-of-flight ion cyclotron resonance detection technique.

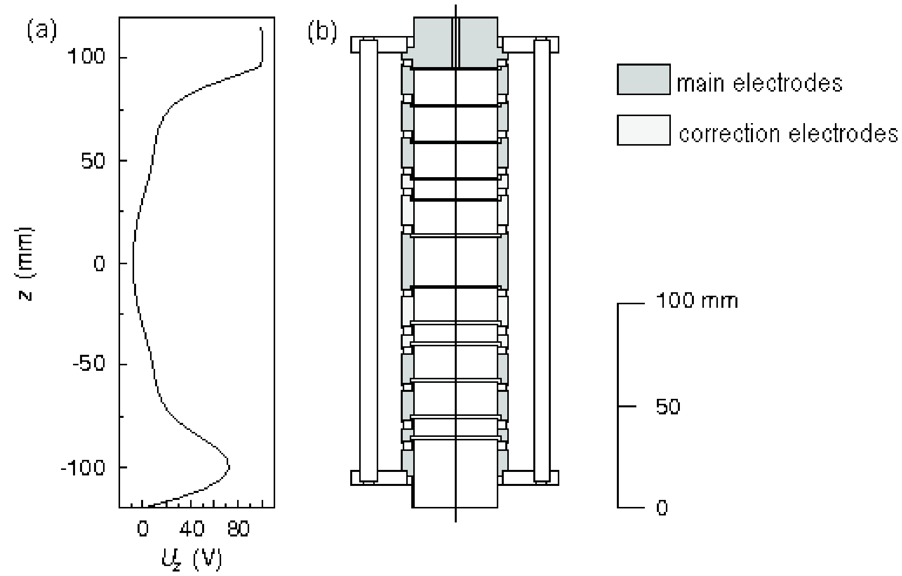

**Figure 3.6:** The harmonic trapping potential (a) in the center of the trap can only be realized by additional correction eletrodes, which are shown in the detailed sketch (b) of the preparation trap.

magnetron excitation is applied to increase the radius of the ion trajectories followed by a quadrupolar rf-field at the cyclotron frequency, which results in a mass selective conversion from the magnetron motion to the modified cyclotron motion, which is damped away rapidly by buffer-gas collisions [Sav91]. With this mass dependent cooling technique, isobaric purification can be achieved with a resolving power of typically $m/\Delta m \approx 10^5$. In addition the emittance of the ions can be improved dramatically to ensure optimal and reproducible starting conditions for the injection in the precision trap.
For optimization purposes cooling resonances are recorded on an MCP detector located behind the preparation trap. They are obtained by varying the quadrupolar frequency around the cyclotron frequency. An example will be shown in Chap. (5.2.4).

### 3.1.4 Precision trap

The hyperbolic precision trap is installed in the bore of a superconducting magnet with $B = 5.9$ T. Being placed in ultra-high vacuum of about $10^{-9}$ mbar the precision trap consists of a four-fold segmented ring electrode, endcaps and additional correction electrodes as shown in Fig. 3.7. The voltages applied to the electrodes are listed in Tab. 3.1. Being ejected from the preparation trap with a low energy spread the ion bunches are captured in flight in the precision trap where first a phase-locked dipolar magnetron excitation is applied in order to bring the ions on a defined magnetron radius [Bla03a]. Afterwards a conversion from a pure magnetron motion to a pure modified cyclotron motion is achieved by applying a quadrupolar excitation whereas $\omega_{rf}$ is scanned around the ions´ cyclotron frequency $\omega_c$. This process is mass selective with a resolving power of up to $m/\Delta m \approx 10^7$,

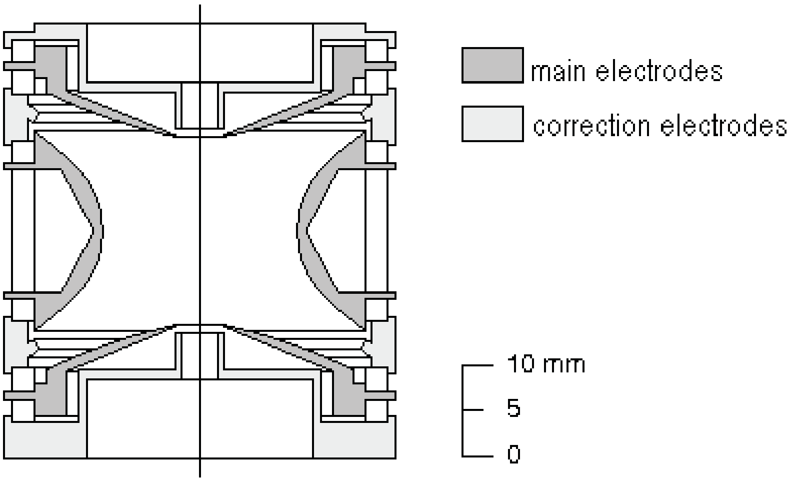

**Figure 3.7:** Detailed sketch of the hyperbolical precision trap. The correction electrodes are necessary to compensate the deformation of the potential due to the segmentation and boreholes in the electrodes.

| Electrode | Voltage/V |
|---|---|
| Lower correction tube | +1.1 |
| Lower endcap | -1.6 |
| Lower correction electrode | -6.6 |
| Ring electrode | -10.0 |
| Upper correction electrode | -6.6 |
| Upper endcap | -1.6 |
| Upper correction tube | +1.1 |

**Table 3.1:** Voltages applied to the electrodes of the precision trap. The ring electrode provides the potential minimum in order to store the ions in the center of the trap. For this purpose a high-precision, high-stability voltage source is used.

depending on the excitation time. Subsequently the ions are ejected and their radial energy is converted into axial energy as they drift through the magnetic field gradient and their time of flight is measured. With this procedure, described in more detail in the next section, the cyclotron frequency $\nu_c$ and therefore the mass $m$ can be determined.

| | Channeltron | MCP |
|---|---|---|
| Efficiency for 1-2 keV ions | >90% | 25%-30% |
| Typical gain at 2.5 kV | $5 \cdot 10^7$ | $5 \cdot 10^7$ |
| Impedance | 40 - 120 MΩ | 66 - 400 MΩ |
| Working pressure | $10^{-6}$ mbar | $10^{-6}$ mbar |
| Dark count rate | <0.05 cps | 2 cps |
| Max. count rate | $10^6$ Hz | $10^7$-$10^8$ Hz |
| Pulse width /dead time | $\sim$ 25 ns | $\sim$ 2 ns |
| Rise time | $\sim$ 5 ns | $\sim$ 0.5 ns |
| Aperture plate size (radius) | 5.6 mm | 5 to 25 mm |
| Cost | 600 € | 600 € per plate |

**Table 3.2:** Typical characteristics of a channeltron and an MCP detector. The main advantage is the high efficiency of the channeltron in comparison to the energy dependent efficiency of the MCP. The dead time for an MCP depends on the diameter of the channels.

### 3.1.5 Time-of-flight ion cyclotron resonance detection

The frequency determination at ISOLTRAP is realized by the destructive time-of-flight technique [Kön95b], which is described in the following. In order to detect the ions, two devices are used: either a micro-channel plate or a channeltron detector. For both devices based on the detection of electron avalanches the characteristics are listed in Tab. 3.2.
One possibility to determine the cyclotron frequency of an ion is given by the time-of-flight technique (see Fig. 3.8), which provides spectra as shown in Fig. 3.9. First, a phase-locked dipolar magnetron excitation is applied to the ring electrode of the precision trap [Bla03a]. Once the ions are on a certain magnetron radius (at ISOLTRAP ideally at about $\rho_- = 0.7$ mm) a quadrupole excitation is applied, whereas the excitation frequency $\nu_{\rm rf}$ is scanned around the cyclotron frequency $\nu_c$. Ideally the excitation time is set to $T_{\rm rf} = 2.8 \cdot t_{1/2}$ with $t_{1/2}$ beeing the half-life of the nuclide of interest. However, for long-lived or stable species an excitation time of typically $T_{\rm rf} = 900$ ms is chosen. The amplitude of the excitation is chosen such that in resonance, i.e. at $\nu_c$ a full conversion from a pure magnetron to a pure modified cyclotron motion is achieved. For nonresonant excited ions the conversion is not complete so that they have less radial energy. At the end of the excitation time the ion bunch is still on the same radius but since $\nu_+ \gg \nu_-$ the radial energy is increased by orders of magnitude. The orbital magnetic moment of the ions $\vec{\mu}$, which is proportional to the radial energy, increases with the conversion and couples to the magnetic field gradient when the ions are ejected out of the trap resulting in an acceleration along the magnetic field axis. Using this process the radial energy is transferred into axial energy, which means ions in resonance are faster than those out of resonance.
Theoretically the time-of-flight (ToF) spectrum can be described with:

$$T(\omega_{\rm rf}) = \int_{z_{trap}}^{z_{detector}} \sqrt{\frac{m}{2(E_0 - q \cdot U(z') - \mu(\omega_{\rm rf}) \cdot B(z'))}} dz' \tag{3.1}$$

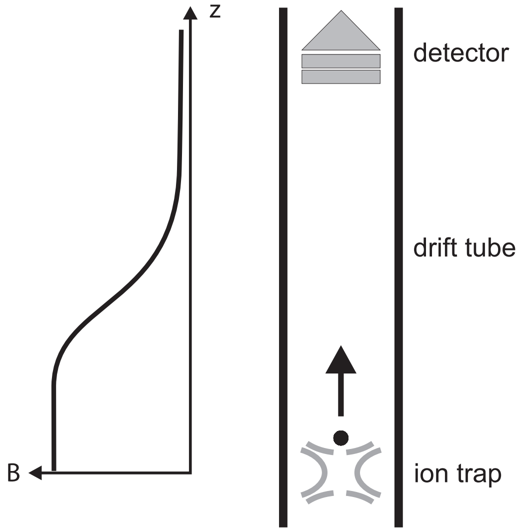

**Figure 3.8:** Principle of the time-of-flight ion cyclotron resonance detection technique [Grä80]. The magnetic field gradient (left) and the drift section (right) are shown.

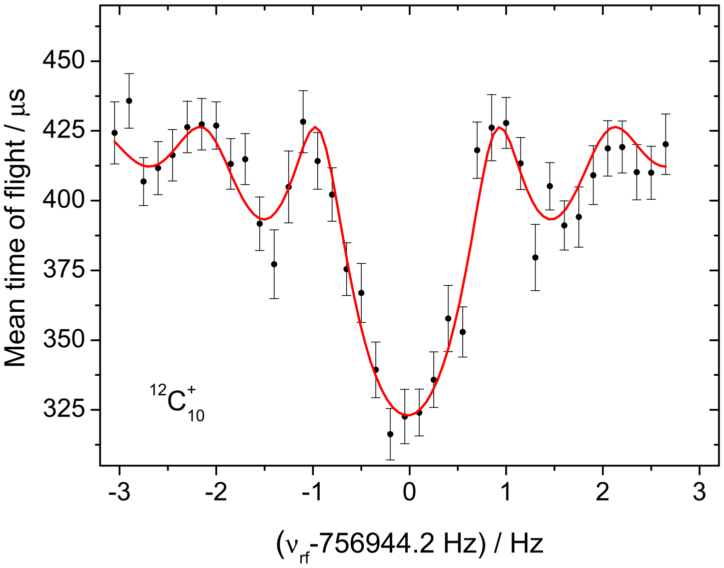

**Figure 3.9:** Time-of-flight spectrum of $^{12}\mathrm{C}^+_{10}$ with an excitation time of $T_{\mathrm{rf}} = 900$ ms. The lineshape reflects the Fourier transform of the applied rectangular excitation signal. The solid line is a fit of the theoretical lineshape to the data [Kön95a].

where $U(z')$ and $B(z')$ are the electric and magnetic field, respectively, along the ion trajectory [Kön95a]. By fitting the ToF spectrum with the theoretical line profile, the cyclotron frequency, (given at the frequency of the minimum time of flight,) can be very precisely determined. The resolving power of these measurements is limited by the duration $T_{\mathrm{rf}}$ of the quadrupolar excitation and is given by [Muk04]:

$$R = \frac{m}{\Delta m} = \frac{\nu}{\Delta \nu} \approx 1.25 \cdot \nu_c \cdot T_{\mathrm{rf}}. \tag{3.2}$$

Typical values for $T_{\mathrm{rf}} = 900$ ms, and $\nu_c = 1$ MHz ($A = 100$) are $R \approx 10^6$.

### 3.1.6 Measurement timing sequence

The measurement cycle starts with the proton trigger as shown in Fig. 3.10. Ions with energies up to 60 keV are created and the ion beam is directed to the buncher where the ions are trapped and accumulated. The ion bunches are guided through the transferline towards the preparation trap. In front of the trap they are slowed down by a pulsed cavity to an energy of about 100 eV. A capture pulse is applied to the lowest endcap in order to trap the ion bunches in flight. Within a so-called axial cooling time the amplitudes of the ion motion is reduced by buffer gas cooling, which is very important for further excitation steps. Then, a dipolar magnetron excitation is applied to increase the magnetron radius. Subsequently, the magnetron motion is converted into a modified cyclotron motion by coupling these eigenmotions via a quadrupolar cyclotron excitation. Before they are ejected out of the preparation trap, a radial cooling is implemented for further energy loss by buffer gas collisions.

Finally, the ions are captured in flight in the precision trap, where a dipolar phase-locked magnetron excitation is applied. Afterwards the magnetron motion is converted to a modified cyclotron motion realized by a quadrupolar rf field, whereas the excitation frequency $\nu_{\mathrm{rf}}$ is varied around the cyclotron frequency $\nu_c$. Then, the extraction pulse ejects the ions and triggers the data acquisition. Depending on the excitation time the duration of each cycle is about 1 s or more.

## 3.2 Mass determination

### 3.2.1 Measurement principle

The measurement of the cyclotron frequency $\nu_c = qB/(2\pi m)$ allows to calculate the mass $m$ as long as the charge state $q$ and the magnetic field strength $B$ are known. Calibrating the magnetic field with a reference measurement of an ion with a well-known mass, the formula

$$m = \frac{\nu_c^{ref}}{\nu_c} \cdot (m_{ref} - m_e) + m_e, \tag{3.3}$$

where $m_e$ is the mass of the electron, leads to the mass of the ion of interest.

Due to the fact that the magnetic field is drifting in time, the reference measurements have to be done as close in time as possible. Therefore, they are performed before and

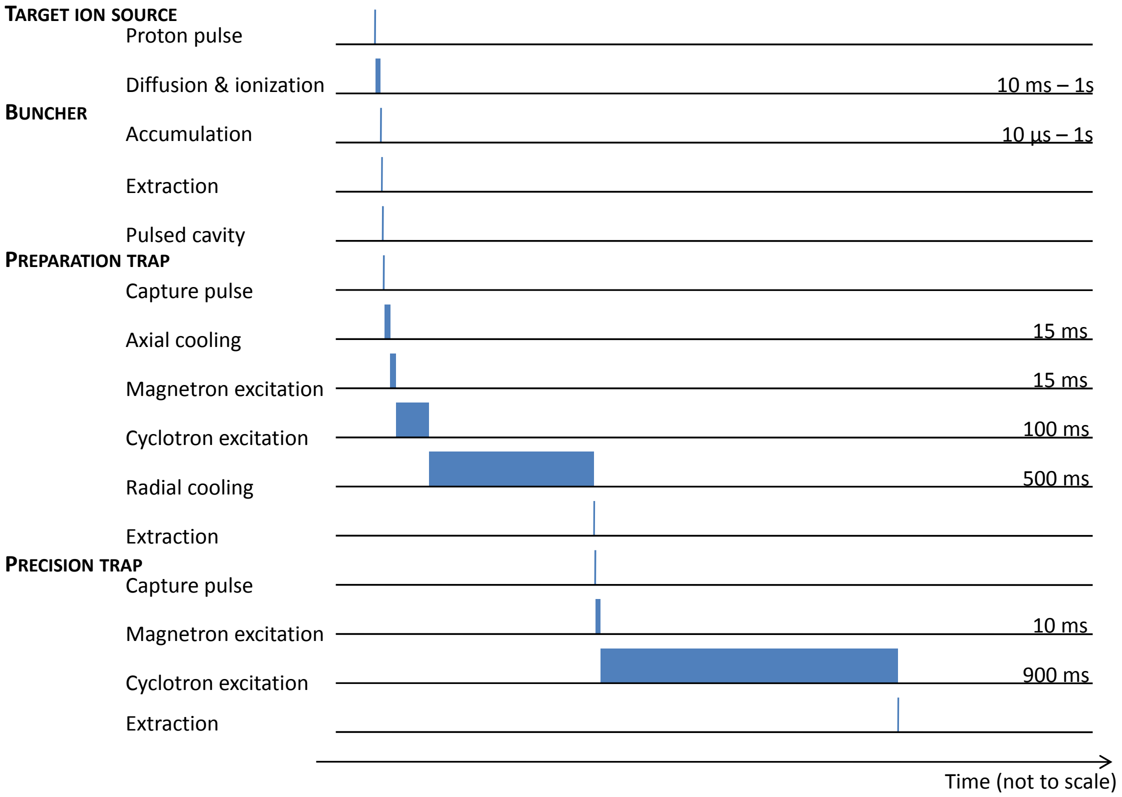
TARGET ION SOURCE
Proton pulse
Diffusion & ionization
10 ms – 1s
BUNCHER
Accumulation
10 µs – 1s
Extraction
Pulsed cavity
PREPARATION TRAP
Capture pulse
Axial cooling
15 ms
Magnetron excitation
15 ms
Cyclotron excitation
100 ms
Radial cooling
500 ms
Extraction
PRECISION TRAP
Capture pulse
Magnetron excitation
10 ms
Cyclotron excitation
900 ms
Extraction
Time (not to scale)

**Figure 3.10:** The timing of the signals for the measurement procedure is depicted. Each cycle is triggered by the proton pulse. After the ionization the quasi-continuous ion beam is passing the buncher. After an accumulation time ion bunches are guided to the tandem Penning trap system. For more details see text.

after each frequency measurement of the ion of interest, which allows a linear interpolation of the magnetic field to the time when the cyclotron frequency at the ion of interest has been measured.

## 3.2.2 Uncertainties in the mass determination

### Statistical uncertainties

Statistical uncertainties in determining the cyclotron frequency from a recorded time-of-flight resonance are connected to the number $N$ of detected ions as well as to the excitation time $T_{\text{rf}}$ [Kel03] via

$$\sigma(\nu_c) \propto \frac{1}{\sqrt{N} \cdot T_{\text{rf}}}. \tag{3.4}$$

Concerning statistical uncertainties a long excitation time and a collection of many particles allow to decrease the uncertainty. Due to the fact that some of the systematic uncertainties, which will be discussed in the following chapter, increase in time one has to find a compromise solution.

### Systematic uncertainties

Several systematic uncertainties contribute to the final uncertainty of the mass value for the ion of interest:

- Presence of contaminants: Typically there are more than 10 ions stored in the precision trap and Coulomb interactions influencing the ion motion have to be considered. As long as the ions are all of the same species no frequency shift will be measured. In case of different ion species ($m_1 \neq m_2$) a frequency shift $\Delta\nu_c$ is observed, which is increasing with the number of contaminant ions in the trap [Bol92]. Therefore, the resonances are taken with only a few ions ($N \leq 5$) in the trap which reduces the shift. Additionally a procedure called z-class-analysis is applied, where $\nu_c$ is determined for events with different numbers of ions in the trap. Based on this procedure the value for $\nu_c$ with only one ion in the trap can be extrapolated [Kel03].

- Long-term drift in the magnetic field: Temperature and pressure fluctuations in the ISOLDE hall are influencing the magnetic field. These short term changes are minimized by a temperature and pressure regulation system [MJ08] installed at ISOLTRAP. In addition a long term drift of the magnetic field due to the steady decrease of the current in the superconducting coils leads to a shift of $\delta B/\delta t \cdot 1/B = 2.3 \cdot 10^{-9}/h$ [Kel03]. The influence of this uncertainty is kept small since measurement times are usually limited to 1-3 h of course limiting vice versa the maximum of the ions that can be collected in the resonance.

- Mass-dependent shift: Systematic studies using carbon cluster ions [Kel03] have shown that a mass-dependent uncertainty is present at ISOLTRAP. Increasing approximately linearly with the mass difference between the ion of interest and the reference ion the value was determined to be: $1.6 \cdot 10^{-10}/u \cdot (m - m_{ref})$. Since this effect is based on trap imperfections, e.g. the misalignment of the magnetic field with respect to the symmetry axis of the trap, an application of the invariance theorem can help to understand this effect in more detail (see Chap. 6).

- Residual uncertainty of unknown source: Limiting the precision of measurements performed at ISOLTRAP, the residual uncertainty for a frequency ratio of

  $$\frac{u_{res}(r)}{r} = 8.9 \cdot 10^{-9}$$

  was determined by systematic studies using carbon cluster ions [Kel03].

The total uncertainty is obtained by adding the individual uncertainties mentioned above in quadrature.

# Chapter 4

# Beamtimes at ISOLTRAP in 2008

In 2008 several beamtimes were performed at ISOLTRAP. In 55 eight-hour online shifts over 20 masses have been determined, whereas several masses were measured for the first time. All investigated nuclides, their half-lives, the ISOLDE production yield, as well as the mass uncertainties as given in the Atomic-Mass Evaluation AME 2003 [Aud03] are listed in Tab. 4.1. Within the present thesis no mass evaluation was performed due to the limited time available after the online running period. Since the beamtime preparation as well as the accomplishment of the mass measurements were also part of the project, a summary of the beamtimes and their physics motivation is given in the following.

### Search for new candidates for the neutrino-oriented mass determination by electron-capture (IS 473)

The combination of ultra-precise mass measurements and cryogenic micro-calorimetry for atomic de-excitation measurements is one possibility to determine a new upper limit for the mass of the electron neutrino, which is presently at 225 eV, and thus compared to the limit of the electron antineutrino of 2.3 eV (95% c.l.) two orders of magnitude larger [Wei06]. The mass measurements allow to determine the $Q$-value for an electron capture process via mass determination of the mother and daughter nuclides whereas cryogenic micro-calorimeters are able to detect the energy release from all atomic de-excitations except the energy of the neutrino. Therefore, the difference of these two results lead to the total energy of the electron neutrino. To obtain an upper limit for the neutrino mass the fraction of its energy in comparison to the energy release of the atomic de-excitations has to be as small as possible. There are only very few candidates around the nuclei chart with a $Q$-value of less than 100 keV, among them $^{163}$Ho, $^{194}$Hg and $^{202}$Pb. However, the uncertainty of the masses of these nuclides as well as their daughter nuclides is too large to be sure, whether an improvement of the upper limit of the electron neutrino mass is possible or not. To this end the masses of $^{194}$Au, $^{194}$Hg and $^{202}$Pb were measured at ISOLTRAP. The $Q$-value for the ground-ground state transition of $^{194}$Hg to $^{194}$Au was measured, but it is still too large for a determination of an upper limit of the electron neutrino mass.

| Nuclide | Half-life | Yield at ISOLDE ions/$\mu$C | Mass Excess AME2003 /keV |
|---|---|---|---|
| $^{126}$Cd | 515(17) ms | $8.9 \cdot 10^5$ | -72330(50) |
| $^{128}$Cd | 280(49) ms | $1.3 \cdot 10^5$ | -67290(290) |
| $^{136}$Xe | stable | $7 \cdot 10^8$# | -86425(7) |
| $^{137}$Xe | 3.818(0.013)m | $6.2 \cdot 10^8$ | -82379(7) |
| $^{138}$Xe | 14.08(0.08) m | $5.7 \cdot 10^8$ | -80150(40) |
| $^{139}$Xe | 39.68(0.14) s | $5 \cdot 10^8$ | -75644(21) |
| $^{140}$Xe | 13.60(0.10) s | $3.5 \cdot 10^8$ | -72990(60) |
| $^{141}$Xe | 1.73(0.01) s | $5.9 \cdot 10^7$ | -68330(90) |
| $^{142}$Xe | 1.22(0.02) s | $3.7 \cdot 10^7$ | -65480(100) |
| $^{143}$Xe | 511(6) ms | $6.6 \cdot 10^6$ | -60450#(200#) |
| $^{144}$Xe | 388(7) ms | $9.9 \cdot 10^5$ | -57280#(300#) |
| $^{145}$Xe | 188(4) ms | $2.6 \cdot 10^4$ | -52100#(300#) |
| $^{146}$Xe | 146(6) ms | $1.8 \cdot 10^3$ | -48670#(400#) |
| $^{194}$Hg | 440(80) y | $5 \cdot 10^7$ | -32193(13) |
| $^{194}$Au | 38.02(0.10) h | $10^5$# | -32262(10) |
| $^{202}$Pb | 52.5(2.8) ky | $4.6 \cdot 10^6$ | -25934(8) |
| $^{220}$Rn | 55.6(0.1) s | $1.9 \cdot 10^7$ | 10613.4(2.2) |
| $^{223}$Rn | 24.3(0.4) m | $2.5 \cdot 10^6$ | 20300#(300#) |
| $^{224}$Rn | 107(3) m | $2.8 \cdot 10^6$ | 22440#(300#) |
| $^{225}$Rn | 4.66(0.04) m | $1.7 \cdot 10^5$ | 26490#(300#) |
| $^{226}$Rn | 7.4(0.1) m | $1.1 \cdot 10^5$ | 28770 #(400#) |
| $^{227}$Rn | 20.8(0.7) s | $1.3 \cdot 10^4$ | 32980#(420#) |
| $^{228}$Rn | 65(2) s | $3.7 \cdot 10^3$ | 35380# (410#) |
| $^{229}$Rn | unknown | 100# | unknown |

**Table 4.1:** List of nuclides measured at ISOLTRAP in 2008 with half-lives, yield at ISOLDE and mass excess values as given in the Atomic-Mass Evaluation AME2003 [Aud03]. Extrapolated values are marked by #.

### Investigation of the proton-neutron interaction by high-precision nuclear mass measurements (IS 461)

One of the main physics programs at ISOLTRAP is devoted to mass measurements of short-lived nuclides for nuclear structure studies. Proposed mass measurements include the nuclides $^{122-130}$Cd, $^{138,140}$Xe, $^{207-210}$Hg and $^{223-225}$Rn with a mass precision below 10 keV. These masses are important, e.g., to understand the average interaction between the last proton and last neutron, which can be calculated using the so-called $\delta V_{pn}$ values, which are double-mass differences. For even-even nuclides the $\delta V_{pn}$ values can be calculated via:

$$\delta V_{pn}(Z,N) = \frac{1}{4}[\{B(Z,N) - B(Z,N-2)\} - \{B(Z-2,N) - B(Z-2,N-2)\}], \quad (4.1)$$

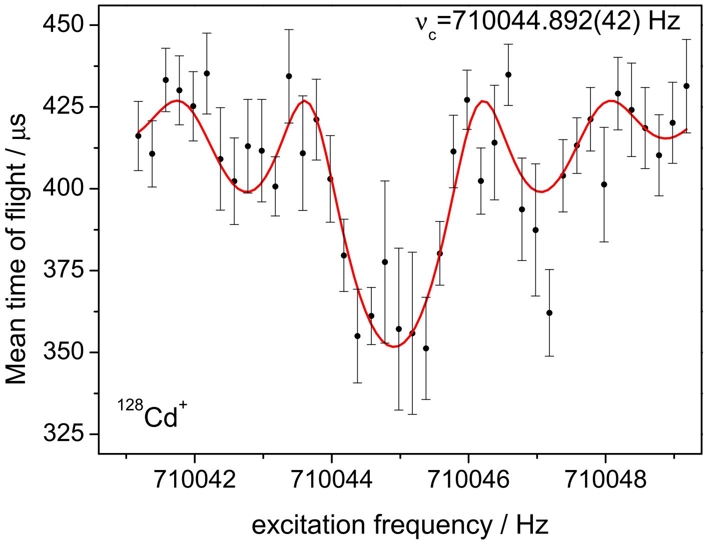

**Figure 4.1:** Time-of-flight spectrum of $^{128}$Cd$^+$ with an excitation time of $T_{\mathrm{rf}} = 600$ ms. $^{128}$Cd is a $\beta$-emitter 16 neutrons away from stability with a half-life of only $t_{1/2} = 280$ ms. The solid line is a fit to the theoretical line shape to the data [Kön95a].

where $B(Z,N)$ is representing the binding energy:

$$B(Z,N) = (Nm_n + Zm_p - m(Z,N))\,c^2. \tag{4.2}$$

Here, $m_n$ and $m_p$ are the neutron and proton masses, respectively, and $m(Z,N)$ the mass of the nuclide with $Z$ protons and $N$ neutrons. In 2008 $^{126,128}$Cd (for an example of a $^{128}$Cd$^+$ time-of-flight ion cyclotron resonance see Fig. 4.1), $^{136-146}$Xe and $^{223-229}$Rn were measured, which allows to calculate new $\delta V_{pn}$ values. Eleven of these masses were determined for the first time. Unique pattern in the $\delta V_{pn}$ values was revealed in the Rn chain, which might be connected to the octupole deformation known in this region of the nuclear chart [Nei09]. In addition, for the first time a new nuclide, $^{229}$Rn, was discovered via Penning trap mass spectrometry, and its time-of-flight spectrum is presented in Fig. 4.2.

### Decay studies and mass measurements on isobarically pure neutron-rich Hg isotopes (IS 463)

The aim was to perform mass measurements followed by $\beta$- and $\gamma$-decay studies in order to determine the binding energies of Hg isotopes beyond $N$=128 as well as energies, spins and parities of their daughter Tl nuclides. These values will provide input for mass models and the nuclear shell-model, which describe the proton-neutron interaction in this region of the nuclear chart. The reason why the region 50<$Z$<82 and $N$>126 is not well studied are large contaminations due to surface-ionized francium. ISOLTRAP allows to separate isobars and even isomeres [Sch01, Bla04, Roo04, Web05] and a recently installed prototype

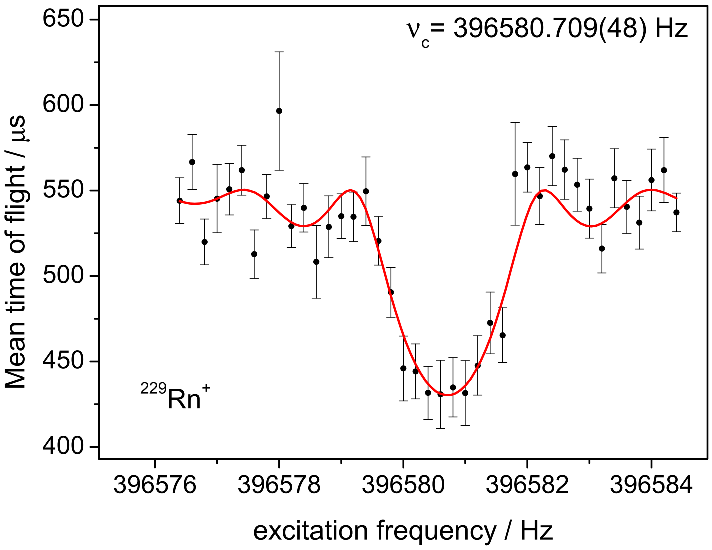

**Figure 4.2:** Time-of-flight spectrum of $^{229}$Rn$^+$ with an excitation time $T_{\mathrm{rf}} = 600$ ms. The half-life of $^{229}$Rn was determined using the ISOLDE tape station to $t_{1/2}$=12.0±1.2 s. The solid line is a fit to the theoretical line shape to the data [Kön95a].

tape station system behind the precision trap allows also to perform decay spectroscopy on pure beams. Unfortunately, the requested Hg beam could not be delivered by ISOLDE due to problems with the target and the ion source. To use the allocated time effectively beams around mass number $A = 213$, where the largest Fr contamination is expected, were used and the purifying capabilities of ISOLTRAP in this mass range were successfully investigated. Also, to test the decay system in online conditions, a $^{138}$Xe beam was purified, reaccelerated, and implanted on the tape, and $\beta$- and $\gamma$-spectra were taken. Presently the ISOLDE target group is investigating the reason for the problem with the Hg beam. On the ISOLTRAP side, optimization steps were done on ion transfer and tape transport.

# Chapter 5

# Setup of a carbon-cluster laser ion source

## 5.1 Off-line ion sources at ISOLTRAP

Ions for test measurements and for the magnetic field calibration can be produced at ISOLTRAP by two different off-line ion sources. Alkali elements like $^{39}$K, $^{85,87}$Rb and $^{133}$Cs are created by a surface ion source, which is installed in front of the buncher perpendicular to the ISOLDE beamline as shown in Fig. 5.1. The continuous ion beam created via thermal emission of the surface ion source is fed into the ISOLDE beamline by bending electrodes. Due to the fact that the surface ion source is held at a potential of 60 kV, similar starting conditions as for the ISOLDE beam are provided. Afterwards the ions are accumulated and cooled in the buncher. The second off-line ion source supplies a wide mass range of laser ionized carbon-clusters. The fact that the production mechanism leads to bunched ion clouds allows the installation of the laser ion source behind the buncher. One advantage of the carbon-cluster laser ion source is that the mass of the produced ions is known exactly since the atomic mass unit is defined to be one twelfth of the mass of a $^{12}$C atom in ground state [Emi95]. Furthermore, this kind of source provides a dense grid of reference ions, which has already been shown in Fig. 1.1. Therefore, the mass-dependent systematic uncertainty, which is increasing with the difference between the measured and the reference mass, as discussed in Chap. (3.2.2), is reduced. A detailed description of the laser ion source optimized and characterized within this thesis is given in the following.

## 5.2 The ISOLTRAP carbon-cluster laser ion source

The ISOLTRAP carbon cluster ion source is a nonresonant type of laser ion source, i.e. the process is based on laser induced desorption of material with possible fragmentation and ionization of that material.
A pulsed high-intensity laser hits a solid sample, which is in case of the ISOLTRAP laser ion source made of carbon. In the present studies a non-graphitizing glassy carbon,

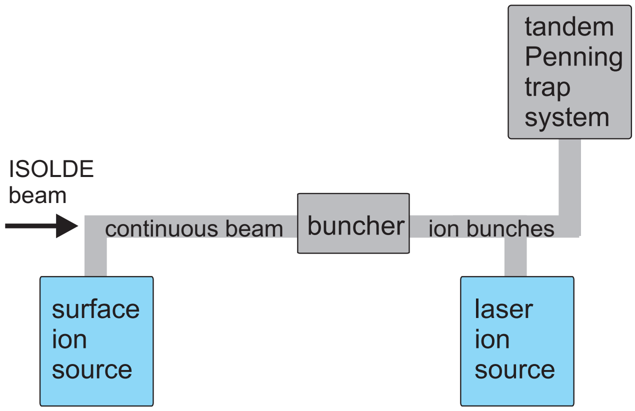
tandem Penning trap system
ISOLDE beam
continuous beam
buncher
ion bunches
surface ion source
laser ion source

**Figure 5.1:** Two off-line ion sources used at ISOLTRAP produce stable ions required for test measurements, optimization of the ion transport and measurement process, as well as for the calibration of the magnetic field strength. On the one hand the surface ion source installed in front of the buncher provides a continuous alkali ion beam and on the other hand bunches of carbon cluster ions are generated by the laser ion source.

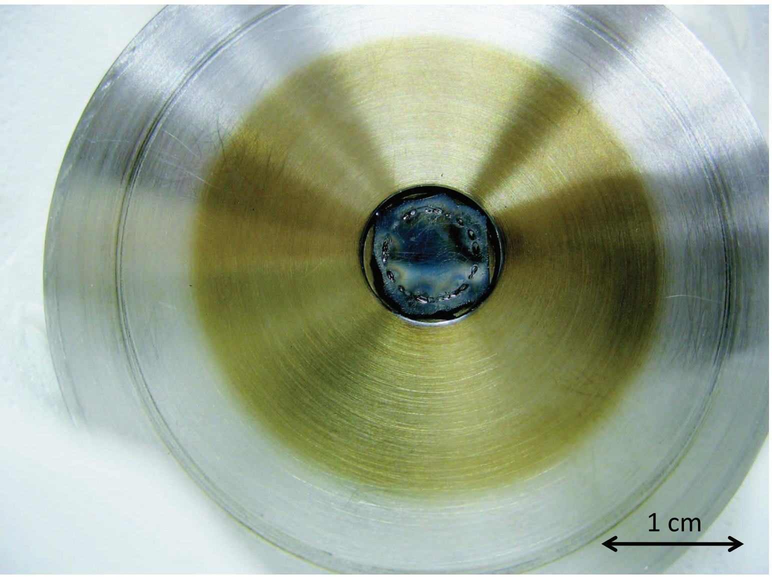

**Figure 5.2:** Photograph of an ISOLTRAP Sigradur pellet glued on a stainless steel sample holder. A circle on the target material formed by many craters is the result of many hours of the laser ablation process. The pellet is continuously rotating (with about 2 Hz) to ensure that the beam is hitting different positions on the Sigradur surface. The surrounding of the solid target is coated by carbon dust.

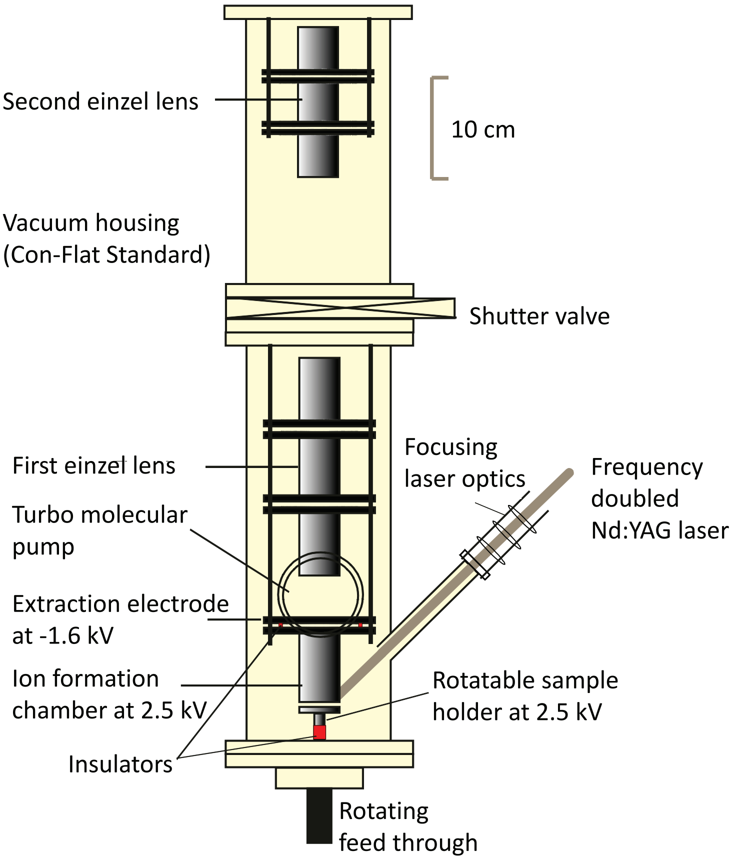
Second einzel lens
10 cm
Vacuum housing
(Con-Flat Standard)
Shutter valve
First einzel lens
Focusing
laser optics
Frequency
doubled
Nd:YAG laser
Turbo molecular
pump
Extraction electrode
at -1.6 kV
Ion formation
chamber at 2.5 kV
Rotatable sample
holder at 2.5 kV
Insulators
Rotating
feed through

**Figure 5.3:** The previous setup was installed in the year 2004 at the ISOLTRAP experiment [Muk04]. Because the shutter valve was too heavy and caused mechanical instability it was taken out, together with the second einzel lens.

Sigradur[1], see Fig. 5.2, was used and carbon atoms or clusters are ablated. They fuse or fragment, and finally get singly- or multiply-ionized in the ablation plume. For ISOLTRAP purposes, the laser properties are chosen such that mostly singly-ionized carbon clusters are created. Since this ionization method is not mass selective, many different systems (atoms, molecules, clusters) can be produced in this way using only one laser, which makes this system relatively cheap and easy to use.

### 5.2.1 Improvements of the original source

The carbon-cluster laser ion source was originally installed at ISOLTRAP in 2004 [Muk04] according to the layout presented in Fig. 5.3. Due to insulation problems and mechanical instabilities some improvements have been performed since then. A photograph of the new setup is shown in Fig. 5.4.

---

[1] trade name, Hochtemperatur Werkstoffe GmbH

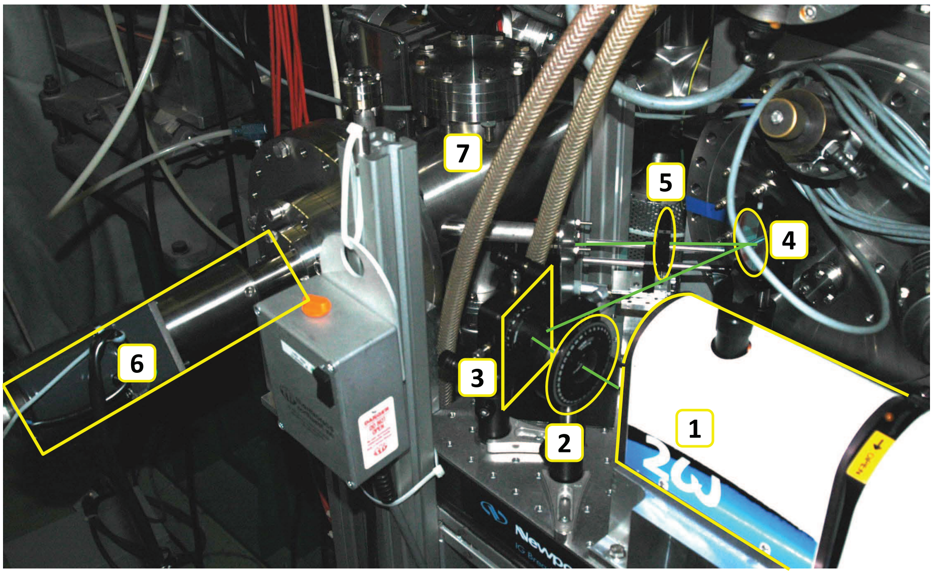

**Figure 5.4:** The close-to-linear polarization of the Nd:YAG laser beam (1) is rotated by a $\lambda/2-$plate (2) and enters then the polarization sensitive beam splitter (3). Next, the laser beam is reflected by a mirror (4) and passes through a focusing lens (5). Afterwards the laser light hits a Sigradur pellet which is rotated by a motor (6) in order to ablate clusters at different pellet positions. The vacuum chamber (7) including the ion optics is attached to the ISOLTRAP beamline.

Fig. 5.5 shows the new arrangement including two new insulators and additional optical elements with which one can adjust the intensity of the laser beam before it is focused on the carbon pellet to perform laser ablation.

The Nd:YAG laser provides high energetic laser pulses which have to be attenuated. Also the method of changing continuously the laser power has been improved. Presently it is realized by a polarization sensitive combination of a lambda-half plate and a beam splitter. In the previous setup the laser beam was attenuated by the choice of a certain delay for the action of the switchable attenuator (Q-switch). This caused problems because the laser is not stable at very low intensities.

### 5.2.2 Laser system

The laser system in use consists of a frequency-doubled pulsed Nd:YAG laser (Brilliant B by Quantel) operating at 1-10 Hz repetition rate and providing 6 ns pulses at 532 nm wavelength. The maximum pulse energy is about 23 mJ, which is by far sufficient to ablate carbon from the Sigradur pellet, and to create a plasma in which the ionization takes place. The pulse energy can be changed by varying the delay time of a switchable attenuator (the Q-switch) in the laser cavity. However, when high attenuation is necessary and the Q-switch delay is set to very short or very long times, the laser intensity becomes unstable and ion production is no longer reliable. Therefore, it is more convenient to set

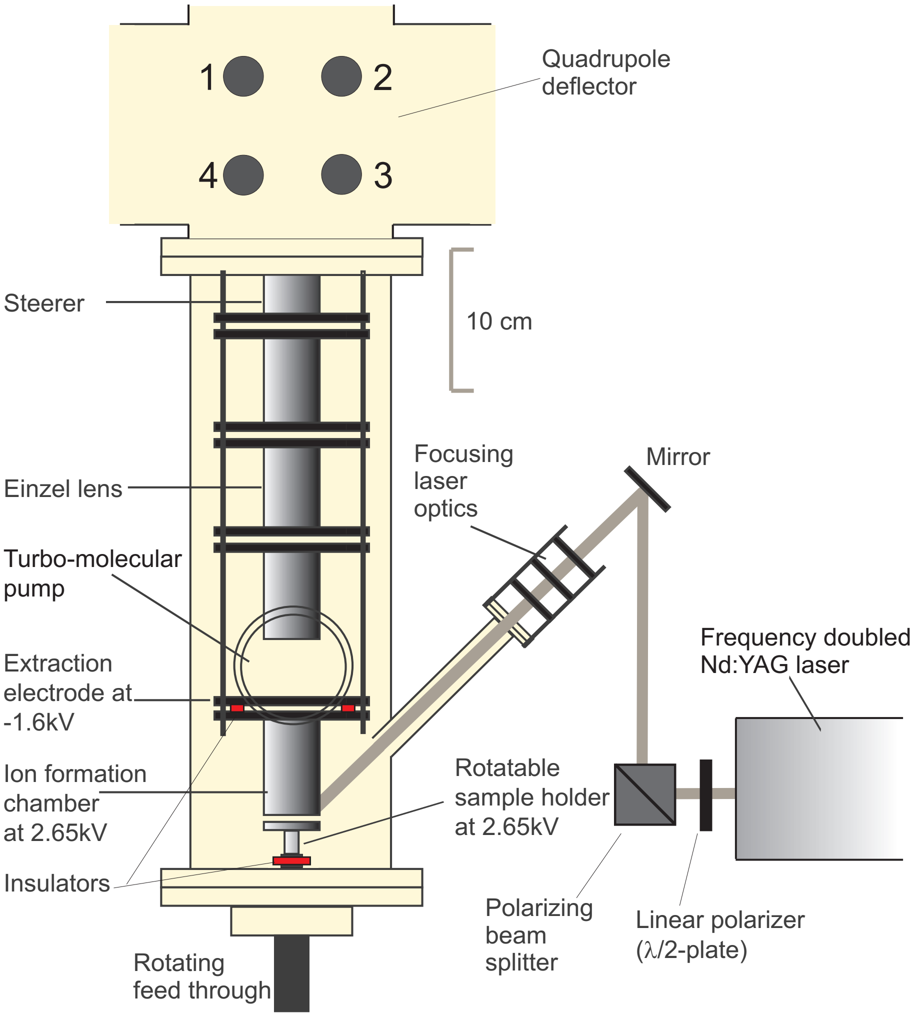
1
2
4
3
Quadrupole deflector
Steerer
10 cm
Focusing laser optics
Mirror
Einzel lens
Turbo-molecular pump
Frequency doubled Nd:YAG laser
Extraction electrode at -1.6kV
Ion formation chamber at 2.65kV
Rotatable sample holder at 2.65kV
Insulators
Polarizing beam splitter
Linear polarizer (λ/2-plate)
Rotating feed through

**Figure 5.5:** The present laser ion source layout. Steerers were implemented and the insulating material was changed to avoid shortcuts in the ion optics system. The laser system was modified by adding an attenuator, which works via polarization selective elements (linear polarizer and polarizing beam splitter).

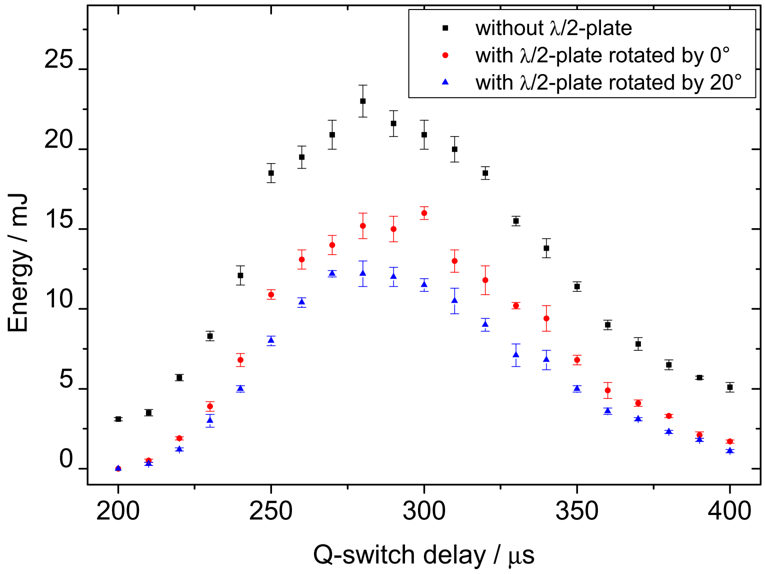

**Figure 5.6:** Laser energy versus Q-switch delay for different settings of the linear polarizer, which is implemented to tune the attenuation of the laser output. The linear polarizer can be rotated continuously. Examples for two rotation angles are shown in red and blue. For the present carbon cluster measurements a Q-switch delay of 355 $\mu$s and a rotation angle of 0° was chosen.

the Q-switch delay such that a high output power is provided which is then attenuated. This is done at the ISOLTRAP source by coupling a linear polarizer ($\lambda/2$-plate) to a polarizing beam splitter, whose reflectivity depends on the polarization of the incoming light. The optimal conditions for a stable and long-term cluster production were found for a Q-switch delay of 355 $\mu$s and on $\lambda/2$-plate at 0°, which corresponds to 6 mJ, see Fig. 5.6. Countrates in the range of zero to 40 ions were observed for several hours without tuning any parameters of the cluster source. By changing slightly either the rotating angle of the $\lambda/2$-plate or the Q-switch delay the countrates stayed in that range for several days.

### 5.2.3 Ion optics

High-energy laser pulses are hitting the Sigradur pellet to create a plasma plume including carbon cluster ions of several masses. In order to prepare the ions in similar conditions like the ions ejected from the buncher, the formation chamber is held at 2.65 kV, which determines the initial ion energy. An extraction electrode held at -1.6 kV attracts the ions into the beamline. Focused by an einzel lens the ion bunches are steered into the center of the quadrupole deflector, which leads the bunch around the corner into the main ISOLTRAP beamline.

| Electrode | Voltage/kV |
|---|---|
| Formation chamber | 2.650 |
| Extraction electrode | -1.600 |
| Lens | 1.870 |
| Steerer | 1.950 |
| Quadrupole deflector 1 | 3.488 |
| Quadrupole deflector 2 | 2.960 |
| Quadrupole deflector 3 | 0.895 |
| Quadrupole deflector 4 | 2.754 |

**Table 5.1:** Voltages applied to the electrodes of the laser ion carbon-cluster source. The value for the potential of the formation chamber defines the initial energy of the ion. Therefore, it has to be adjusted to the energy of the ions coming from the buncher. The ISOLTRAP beamline is optimized on a certain initial energy of the ions, therefore, similar starting conditions are required.

Within this thesis several modifications concerning the extraction insulators were performed. A Marcor ring which was getting easily coated with carbon dust was replaced by a Delrin[2] ring between the extraction electrode and the formation chamber. The second insulation piece, which has been replaced, is mounted between the pellet held at 2.65 kV and the grounded electrical feed through, which is rotating the pellet. The new insulating component is mounted on a spring to compensate misalignments between the pellet and the formation chamber. This insulation part is very important in order to asure that the motor is on ground while the sample holder has to be lifted to the potential of the formation chamber. In 2005 simulations using the program SimIon have been performed to find initial values for the optimization of the voltages. All voltages applied to the electrodes of the cluster source for the present measurements are listed in Tab. 5.1.

### 5.2.4 Carbon-cluster mass spectrum

The produced carbon cluster ions cover a wide mass range as illustrated in Fig. 5.7. In front of the preparation trap several clusters $^{12}\mathrm{C}_n$ for $n \geq 3$ as well as alkali ions were observed. The trapping in the preparation trap was performed for the mass range of $A = n \cdot 12$, with $9 \leq n \leq 25$.

Several cooling resonances as described in Chap. (3.1.6) have been recorded with typical resolving powers of $R = m/\Delta m = \nu_c/\Delta\nu_c = 10^4$. An example of $^{12}\mathrm{C}_{11}^+$ is shown in Fig. 5.8. The trapping was also performed in the precision trap. Employing the detection system behind the precision trap, time-of-flight ion cyclotron frequency resonances for several masses were recorded. Two examples are shown in Fig. 5.9 and Fig. 5.10 for $^{12}\mathrm{C}_{11}^+$ and $^{12}\mathrm{C}_{20}^+$, respectively.

---

[2] Polyoxymethylene plastic, insulating material which is not easily coated by carbon dust

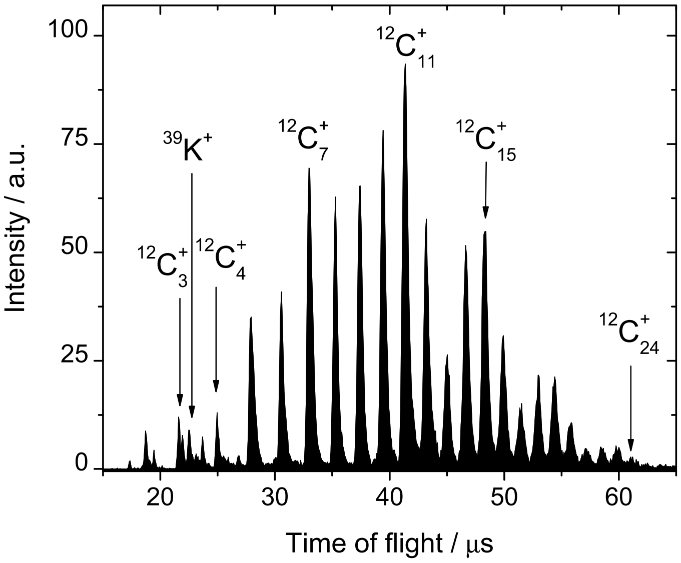

**Figure 5.7:** Time-of-flight spectrum of carbon cluster ions recorded in front of the preparation trap (about 2 m away from the cluster source) on an MCP detector. In this spectrum carbon cluster ions $^{12}\mathrm{C}_n$ from $n = 3$ up to $n = 24$ are identified.

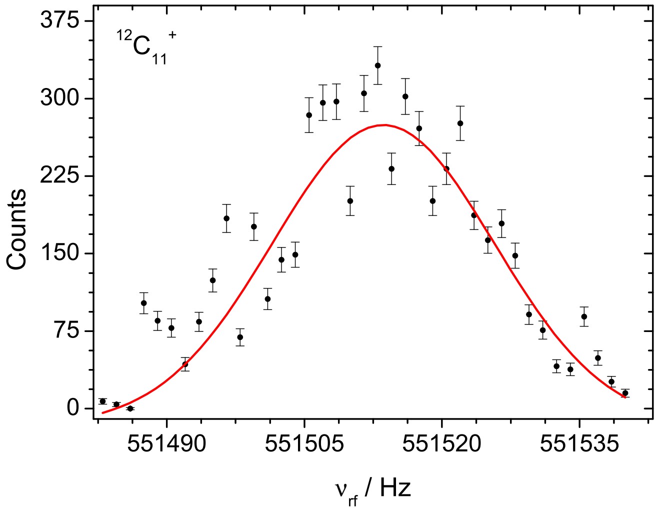

**Figure 5.8:** Cooling resonance of $^{12}\mathrm{C}_{11}^{+}$ with excitation time $T_{\mathrm{rf}}$= 200 ms. The solid line is a Gaussian fit to the data. The center frequency is at $\nu_c$= 515513.6(2) Hz and the FWHM is 28.5(6) Hz. A resolving power of $R \approx 19400$ is obtained.

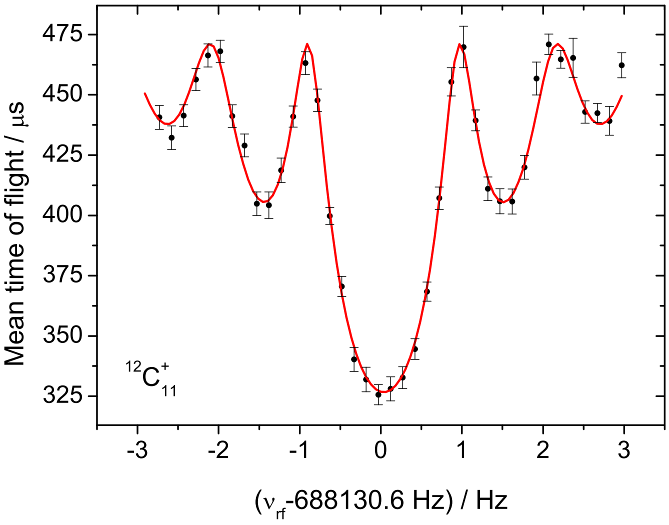

**Figure 5.9:** Time-of-flight ion cyclotron resonance curve for $^{12}C^+_{11}$ with an excitation time of $T_{rf}$= 900 ms. About 3200 ions were recorded. The solid line shows a fit of the theoretical lineshape to the data [Kön95a].

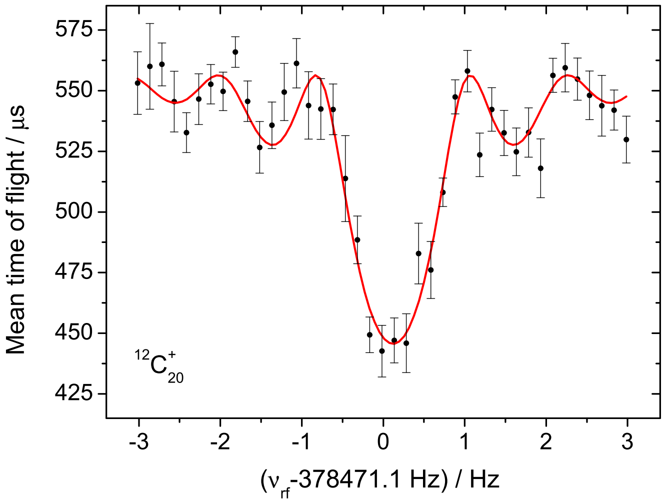

**Figure 5.10:** Same as in Fig. 5.9 but for the carbon cluster $^{12}C^+_{20}$. In total only 1300 ions have been recorded.

# Chapter 6

# Application of the invariance theorem

At ISOLTRAP high-precision mass measurements are performed via the determination of cyclotron frequency ratios:

$$m = (m_{ref} - m_e)\frac{\nu_{c,ref}}{\nu_c} + m_e.$$

The total uncertainty for the mass of the ion of interest contains several contributions [Kel03]. This chapter presents investigations of systematic shifts in the determined cyclotron frequency, which can lower the present limit in precision, and can help to determine the source of these shifts.

In order to investigate systematic uncertainties caused by the misalignment of the magnetic field axis with respect to the symmetry axis of the trap as well as the ellipticity of the electrical field, the measurements presented in the following were performed.

## 6.1 Measurements of the ion motional frequencies in Penning traps

Based on the invariance theorem [Bro86, Gab09] presented in Chap. (2.2.3), one can determine a shift in the cyclotron frequency due to trap imperfections as:

$$\Delta\nu_c = \nu_c^{conv} - \sqrt{\nu_+^2 + \nu_z^2 + \nu_-^2}, \tag{6.1}$$

where $\nu_c^{conv}$ is the conversion frequency between the magnetron and the modified cyclotron frequency $\nu_c^{conv} = \nu_+ + \nu_-$ and $\nu_c^{inv} = \sqrt{\nu_+^2 + \nu_z^2 + \nu_-^2}$ presents the cyclotron frequency according to the invariance theorem. At ISOLTRAP, the mass is determined using the conversion frequency $\nu_c^{conv}$, which in an ideal Penning trap is the cyclotron frequency. Determining the cyclotron frequency $\nu_c^{inv}$ based on the measurement of the three eigenfrequencies one obtains the cyclotron frequency, which is also valid in a real Penning trap [Bro86]. For low ellipticities and tilting angles in the range of $\epsilon \leq 10^{-2}$ and $\theta \leq 10^{-2}$, respectively, Eq. (6.1) can also be written as:

$$\Delta\nu_c \approx \nu_- \cdot \left(\frac{9}{4}\theta^2 - \frac{1}{2}\epsilon^2\right), \tag{6.2}$$

which shows that it is in first order mass-independent. To determine $\Delta\nu_c$ the cyclotron frequencies were measured using both methods, i.e. the measurement of the conversion frequency to obtain $\nu_c^{conv}$ and the measurement of all eigenfrequencies leading to $\nu_c^{inv}$, for three different well-known masses ($^{85}$Rb, $^{12}$C$_{11}$ and $^{133}$Cs) provided by two off-line ion sources.

The measurements performed within this thesis aim to determine the deviation $\Delta\nu_c$ between the measured $\nu_c^{conv}$ and real cyclotron frequency $\nu_c^{inv}$ (derived from the invariance theorem), which can further help to reduce the present limit in the ISOLTRAP systematic uncertainty. Furthermore, the studies should reveal if $\Delta\nu_c$ is mass independent for the ISOLTRAP setup, as given in the invariance theorem. This chapter describes the procedure to determine all four frequencies from Eq. (6.1), followed by the results and the problems, and it concludes with suggestions for future measurements.

In total three sets of measurements for $\nu_c^{conv}, \nu_+, \nu_z$ and $\nu_-$ were performed for $^{85}$Rb, $^{12}$C$_{11}$ and $^{133}$Cs, where the measurement of one set takes several hours, which influences the contribution of the systematic uncertainties (see Chap. (6.2)). The measurements of the frequencies are all based on the determination of the time of flight from the trap to the MCP detector after excitation of the corresponding ion motion. The determination of the conversion frequency $\nu_c^{conv}$ requires a quadrupolar excitation whereas all eigenfrequencies are measured applying a dipolar excitation. For the radial eigenfrequencies as well as the conversion frequency $\nu_c^{conv}$, a conversion from radial in axial energy by coupling of the magnetic moment of the ion to the magnetic field gradient is necessary.

The conversion and the modified cyclotron frequency are contributing mainly to the final value $\Delta\nu_c$ and thus to the uncertainty $\sigma(\Delta\nu_c)$. These two frequencies were measured with higher precision (i.e. longer excitation times were used), since the contributions to $\Delta\nu_c$ should be comparable with the contributions from the magnetron and the axial frequency.

### Measurement of the conversion frequency $\nu_c^{conv}$ and the modified cyclotron frequency $\nu_+$

For the measurement of the conversion frequency $\nu_c^{conv}$ the typical procedure, which was described in Chap. (3.1.5), was applied. For the present studies the excitation scheme applied is shown in Fig. 6.1 (bottom) as well as an example for a cyclotron resonance curve (top).

The determination of the modified cyclotron frequency $\nu_+$ requires a radial dipolar excitation with $\nu_{\mathrm{rf}}$ varied around $\nu_+$. The timing diagram and the corresponding resonance curve are shown in Fig. 6.2.

For both measurements, depending on the ion species, the excitation time was set to $T_{\mathrm{rf}} =$ 1.2 s, 0.9 s and 2 s for $^{85}$Rb, $^{12}$C$_{11}$ and $^{133}$Cs, respectively.

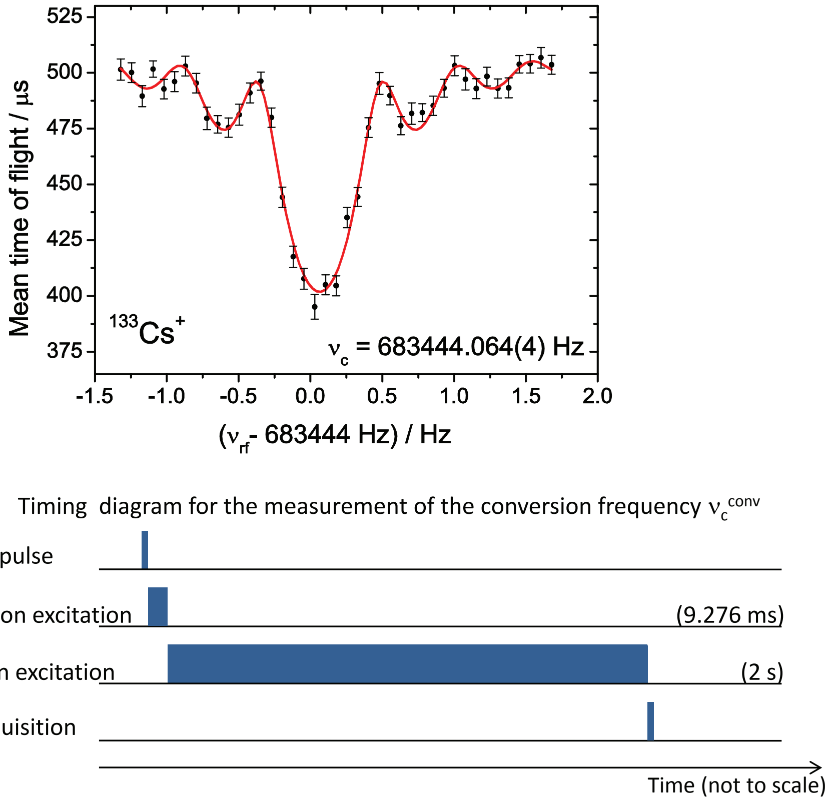

**Figure 6.1:** Time-of-flight spectrum for $^{133}\mathrm{Cs}^{+}$ (top) to determine the conversion frequency with an excitation time of $T_{\mathrm{rf}} = 2$ s. The solid line is a fit to the data points with $\chi^2_{red} \approx 1.06$ [Kön95b]. At the bottom the corresponding timing diagram is presented. The capture pulse is followed by a phase-locked dipolar magnetron excitation to bring the ions on a defined radius. Afterwards a quadrupolar excitation with $\nu_{\mathrm{rf}}$ varied around the cyclotron frequency $\nu_c$ is applied. Finally, the ions are extracted and the data acquisition starts simultaneously.

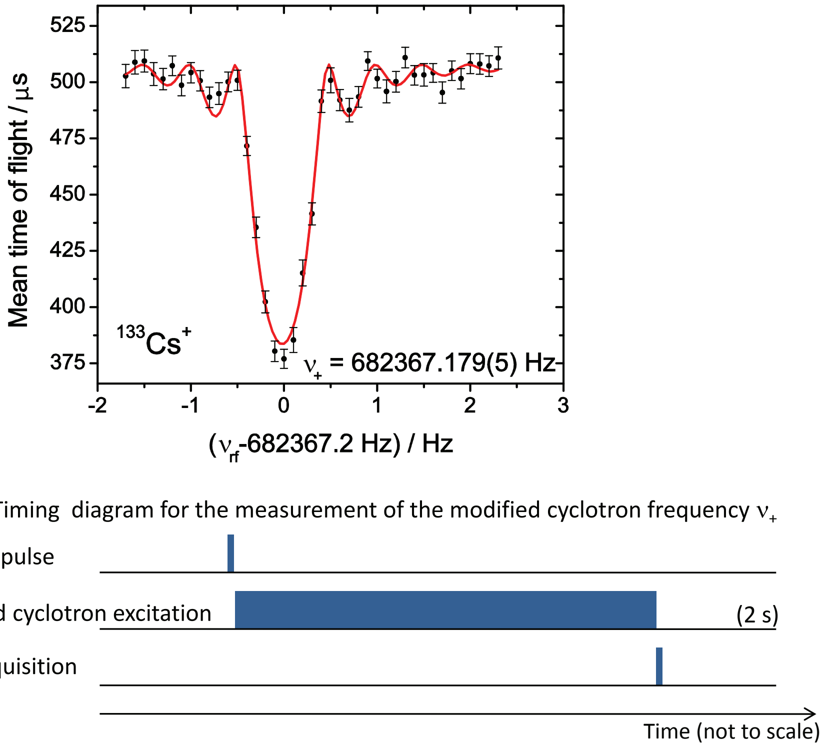

**Figure 6.2:** Time-of-flight spectrum (top) of the $^{133}\mathrm{Cs}^{+}$ modified cyclotron frequency with an excitation time of $T_{\mathrm{rf}} = 2$ s. The solid line shows a fit of the data points with $\chi^2_{red} \approx 1.07$ [Kön95b]. The timing diagram below (example for $^{133}\mathrm{Cs}$) shows the capture pulse followed by a radial dipole excitation where $\nu_{\mathrm{rf}}$ is varied around the modified cyclotron frequency $\nu_{+}$. Finally, the ions are extracted and the data acquisition starts simultaneously.

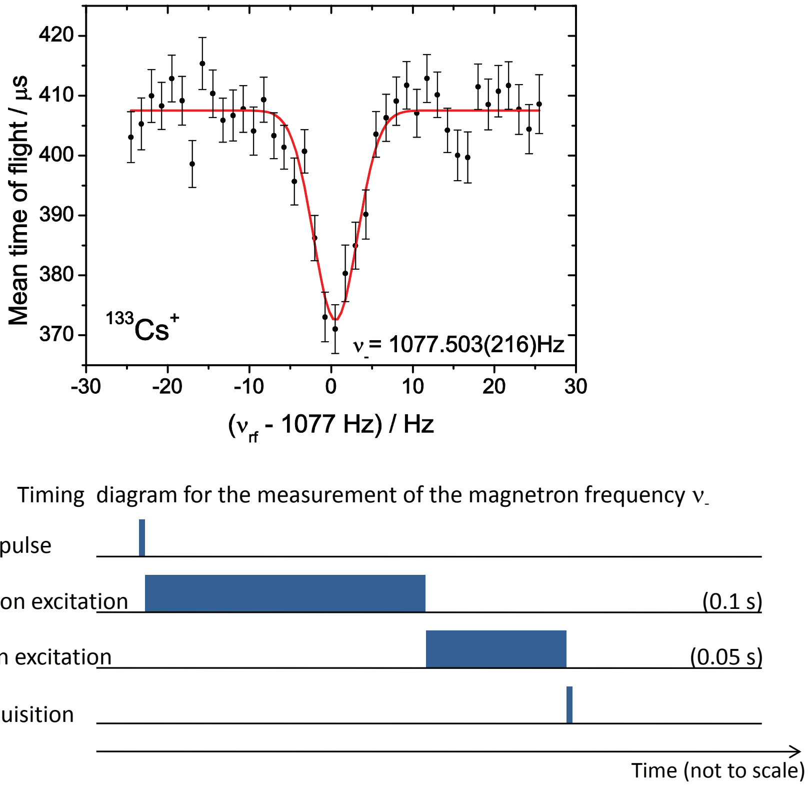

**Figure 6.3:** Time-of-flight spectrum (top) of the $^{133}$Cs$^{+}$ magnetron frequency with an excitation time of $T_{\mathrm{rf}} = 0.1$ s. The solid line is a fit to the data points based on a Gaussian function ($\chi^2_{red} \approx 1.01$). The excitation scheme (bottom) for the determination of the magnetron frequency contains, apart from the capture and the extraction pulse, two excitations. First, a dipolar excitation is applied with $T_{\mathrm{rf}} = 0.1$ s where $\nu_{\mathrm{rf}}$ is varied around the magnetron frequency $\nu_-$. Afterwards a quadrupolar cyclotron excitation converts the magnetron motion of the ions into a modified cyclotron motion within 0.05 s using an excitation amplitude of $a_{\mathrm{rf}} = 4.3\,\mathrm{V}_{pp}$. Therefore a full conversion is achieved. The data acquisition starts with the extraction of the ions.

### Measurement of the magnetron frequency $\nu_-$

First, a phase-locked radial dipolar excitation is applied with the excitation frequency $\nu_{\mathrm{rf}}$ scanned around the magnetron frequency $\nu_-$. This method is sensitive to the excitation amplitude, the frequency and the phase of the applied rf signal (see Fig. 2.5). Varying with the ion species the magnetron excitation is applied for $T_{\mathrm{rf}} = 1.2$ s, 0.4 s and 0.1 s for $^{85}$Rb, $^{12}$C$_{11}$ and $^{133}$Cs, respectively. Afterwards a quadrupolar cyclotron excitation leads to a conversion from the magnetron motion to the modified cyclotron motion whereas the product of excitation time $T_{\mathrm{rf}}$ and the amplitude $a_{\mathrm{rf}}$ was kept constant for all ion species. Then, the ions are extracted and the data acquisition starts as shown in the timing diagram (Fig. 6.3 (bottom)). An example for a time-of-flight resonance for the magnetron frequency is shown in Fig. 6.3 (top). A fit based on a Gaussian function was

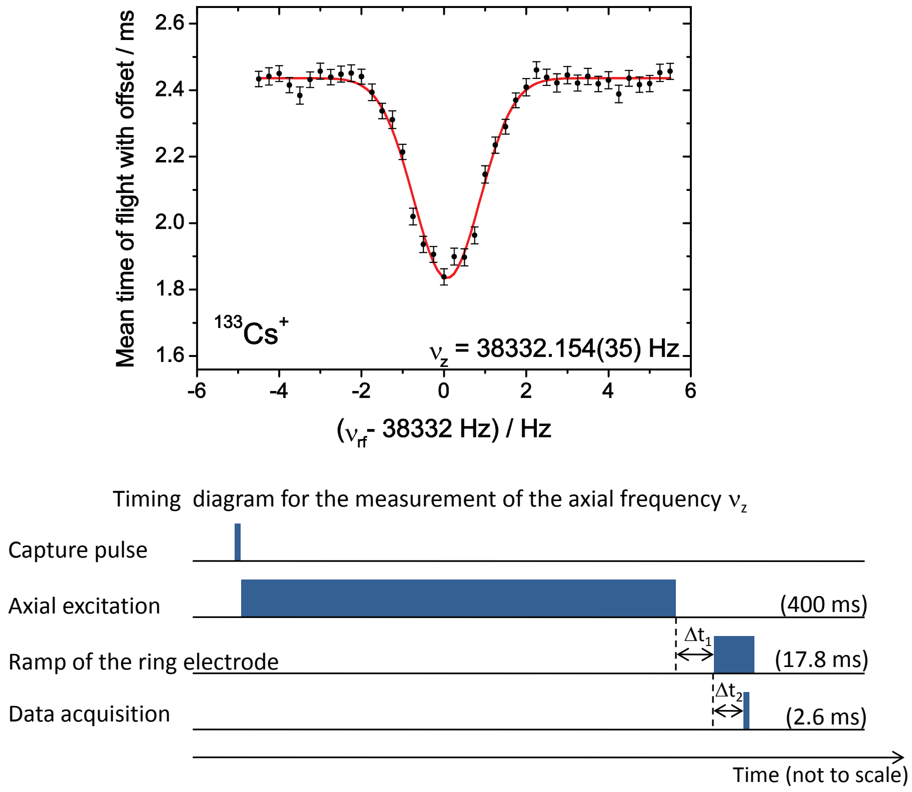

**Figure 6.4:** Time-of-flight spectrum (top) of the $^{133}\mathrm{Cs}^+$ axial frequency with an excitation time of $T_{\mathrm{rf}} = 400$ ms. The solid line shows a fit of the data points based on a Gaussian function ($\chi^2_{red} \approx 0.93$). The timing diagram (bottom) shows the capture pulse followed by an axial dipole excitation with $\nu_{\mathrm{rf}}$ varying around $\nu_z$. After a delay of $\Delta t_1 = 16.6$ ms a ramp potential is applied to the ring electrode in order to allow resonantly excited ions with sufficient energy to leave the trap earlier than nonresonantly excited ions. The data acquisition starts with a delay of $\Delta t_2 = 12.4$ ms after the start of the ramp and takes place for 2.6 ms.

chosen since it is not possible to use the common fit routine for a measurement based on the excitation scheme described above.

### Measurement of the axial frequency $\nu_z$

The measurement of the axial frequency $\nu_z$ differs a lot from the procedures for the determination of the radial frequencies, as shown in the timing diagram in Fig. 6.4 (bottom). A dipolar excitation with $\nu_{\mathrm{rf}}$ varied around the axial frequency $\nu_z$ is applied to the endcaps and causes in resonance an increasing amplitude of the ion motions. The excitation times were set to $T_{\mathrm{rf}}$= 0.1 s, 0.1 s and 0.4 s for $^{85}$Rb, $^{12}\mathrm{C}_{11}$ and $^{133}$Cs, respectively. Depending on the ion species the amplitude had to be adjusted such that a constant product $a_{\mathrm{rf}} \cdot T_{\mathrm{rf}}$ was achieved. The axial excitation is followed by a delay $\Delta t_1 = 16.6$ ms, then a potential

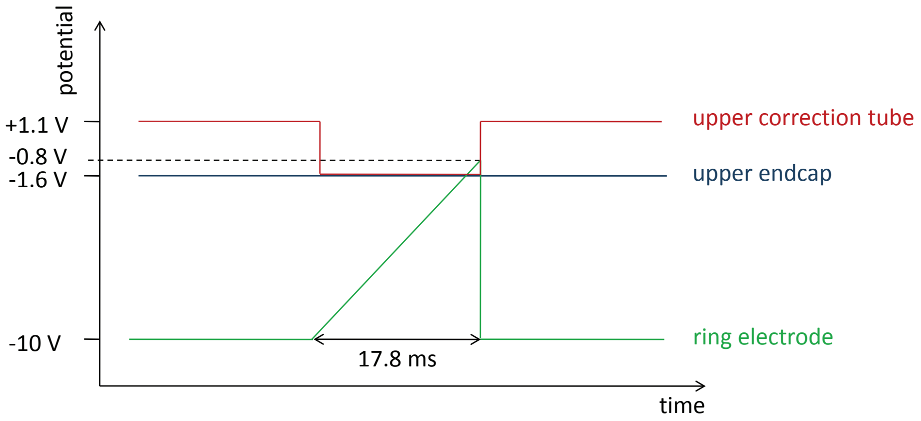

**Figure 6.5:** The potential of the ring electrode is ramped from -10 V to -0.8 V. Therefore, resonantly excited ions with enough axial energy leave the trap earlier then nonresonantly excited ions. In order to avoid the potential wall caused by the upper correction tube, this electrode is adjusted to the potential of the upper endcap while the ramp is applied to the ring electrode.

ramp is applied to the ring electrode. Simultaneously the potential applied to the upper correction tube is lowered to endcap potential (see Fig. 6.5). The data acquisition starts after a delay of $\Delta t_2 = 12.4$ ms after the start of the ramp and takes place for 2.6 ms. Resonantly excited ions have higher axial energy and leave the trap earlier than nonresonantly excited ions. Hence, a time-of-flight spectrum is visible (see Fig. 6.4 (top)). Since it is not possible to apply the common fit routine a fit based on a Gaussian function was used instead.

## 6.2 Experimental results and discussion

### 6.2.1 Results and statistical uncertainties

For three ion species the conversion frequencies and the eigenfrequencies as well as statistical uncertainties are listed in Tab. 6.1. Considering the statistical uncertainty only the conversion and the modified cyclotron frequency were measured with a precision of tens of mHz whereas the axial and the magnetron frequency were determined with a precision in the range of hundreds of mHz. Tab. 6.2 shows $\Delta\nu_c$ (see Eq. (6.1)) and $\Delta\nu_c^{mean}$ for all three ion species, which were obtained as weighted averages of the three data sets. The results are graphically displayed in Fig. 6.6. According to the invariance theorem, the shift $\Delta\nu_c$ is based on field imperfections and misalignment (see Eq. (6.2)). Therefore, for the estimated ellipticity around $\epsilon \approx 0.01$ and tilting angle $\theta \approx 0.01 (\approx 0.6°)$ $\Delta\nu_c$ is expected to be mass independent and equal to around 200 mHz. The measured $\Delta\nu_c$ is indeed in the expected range, but contrary to the invariance theorem predictions it is very different for the three ion species, and $\Delta\nu_c^{mean}$ varies from 100 to 350 mHz. Possible reasons for the large discrepancy of these values are described in the following chapter.

| | | $\nu_c^{conv}$ /Hz | $\nu_+$ /Hz | $\nu_-$ /Hz | $\nu_z$ /Hz |
|---|---|---|---|---|---|
| $^{85}$Rb | Set 1 | 1069741.294(9) | 1068664.933(23) | 1075.988(34) | 47953.874(692) |
| | Set 2 | 1069741.251(15) | 1068664.959(21) | 1075.945(47) | 47954.540(14) |
| | Set 3 | 1069741.228(8) | 1068664.942(14) | 1075.885(28) | 47955.853(560) |
| | $T_{\mathrm{rf}}$/s | 1.2 | 1.2 | 1.2 | 0.1 |
| | | $\nu_c^{conv}$ /Hz | $\nu_+$ /Hz | $\nu_-$ /Hz | $\nu_z$ /Hz |
| $^{12}$C$_{11}$ | Set 1 | 688130.697(13) | 687052.636(13) | 1078.008(207) | 38486.851(396) |
| | Set 2 | 688130.707(15) | 687052.647(12) | 1077.906(131) | 38486.540(340) |
| | Set 3 | 688130.686(14) | 687052.602(19) | 1077.926(109) | 38486.987(426) |
| | $T_{\mathrm{rf}}$/s | 0.9 | 0.9 | 0.4 | 0.1 |
| | | $\nu_c^{conv}$ /Hz | $\nu_+$ /Hz | $\nu_-$ /Hz | $\nu_z$ /Hz |
| $^{133}$Cs | Set 1 | 683444.064(4) | 682367.179(5) | 1077.748(364) | 38831.645(25) |
| | Set 2 | 683444.126(6) | 682367.223(4) | 1076.981(494) | 38332.359(33) |
| | Set 3 | 683444.117(5) | 682367.236(6) | 1077.503(216) | 38332.070(19) |
| | $T_{\mathrm{rf}}$/s | 2.0 | 2.0 | 0.1 | 0.4 |

**Table 6.1:** Three independent sets of measurements for the conversion frequency $\nu_c^{conv}$ and all eigenfrequencies were performed for different ion species: $^{85}$Rb, $^{12}$C$_{11}$ and $^{133}$Cs. Statistical uncertainties are given in brackets. In case that $\chi^2_{red} > 1$ we used the procedure described by the Particle Data Group and multiplied the statistical uncertainty by $\sqrt{\chi^2_{red}}$ [Eid04].

| | | $\Delta\nu_c$/mHz | $\Delta\nu_c^{mean}$/mHz |
|---|---|---|---|
| $^{85}$Rb | Set 1 | 451(40) | 349(34) |
| | Set 2 | 352(27) | |
| | Set 3 | 288(30) | |
| $^{12}$C$_{11}$ | Set 1 | 96(29) | 107(17) |
| | Set 2 | 112(27) | |
| | Set 3 | 113(34) | |
| $^{133}$Cs | Set 1 | 252(7) | 238(7) |
| | Set 2 | 232(7) | |
| | Set 3 | 225(8) | |

**Table 6.2:** Results of the frequency shifts for all data sets as well as mean frequency shifts and statistical uncertainties, which are mainly influenced by the contribution of the conversion, the modified cyclotron and the axial frequency. The influence of the uncertainty of the magnetron frequency is negligible.

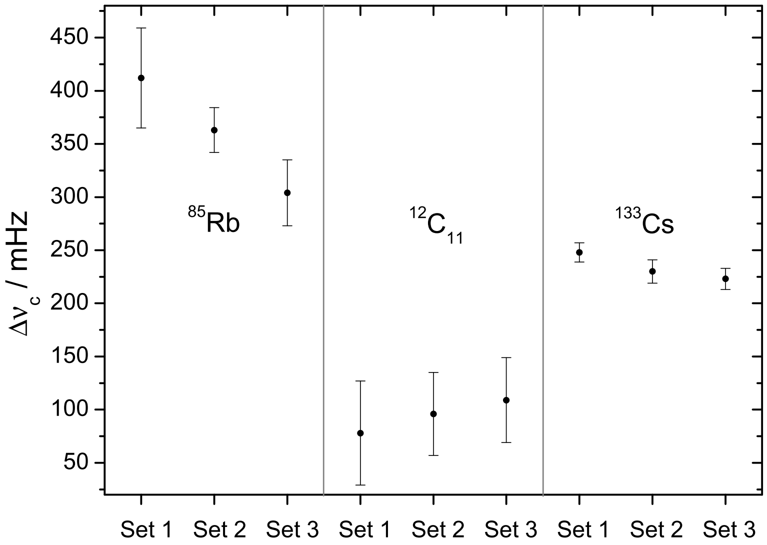

**Figure 6.6:** Cyclotron frequency shifts according to Eq. (6.1) for all three sets recorded for $^{85}$Rb, $^{12}$C$_{11}$ and $^{133}$Cs. The values are extracted from Tab. 6.2.

### 6.2.2 Discussion of systematic uncertainties

Since the results for $\Delta\nu_c$ are different for the three investigated ion species, further effects apart from trap imperfections must be present. Several systematic effects were identified influencing $\Delta\nu_c$, e.g. fluctuations of the magnetic field strength, changes in temperature, voltage fluctuations, and differences in experimental details, such as the ion injection into the trap, causing different ion trajectories, or different excitation amplitudes. Thus the ions probe different field imperfections and misalignments, which can influence any of the four measured frequencies. In the present chapter these effects will be discussed, and explain why the experimental values of $\Delta\nu_c$ are the similar for one, but not for different ion species. The results of the frequency measurements were investigated by applying equations which are valid in ideal Penning traps (see Tab. 6.3):

$$\nu_z = \sqrt{2\nu_+\nu_-}, \tag{6.3}$$

$$\nu_c^{conv} = \nu_+ + \nu_-. \tag{6.4}$$

The fact that the deviations (see Fig. 6.7) are fluctuating correlated, leads to the conclusion that the discrepancies are based on the values of the modified cyclotron frequency $\nu_+$ and the magnetron frequency $\nu_-$ since they are contributing to both equations.

Due to the discrepancies the present chapter will discuss a number of sources, which have an influence on the measurements.

| | | $\nu_z - \sqrt{2\nu_+\nu_-}$ | $\nu_c^{conv} - (\nu_+ + \nu_-)$ |
|---|---|---|---|
| $^{85}$Rb | Set 1 | -1.74(0.69) | 0.37(0.04) |
| | Set 2 | -0.12(0.14) | 0.35(0.05) |
| | Set 3 | 2.53(0.56) | 0.40(0.03) |
| $^{12}$C$_{11}$ | Set 1 | -0.76(0.40) | 0.05(0.21) |
| | Set 2 | 0.75(0.34) | 0.15(0.13) |
| | Set 3 | 0.84(0.43) | 0.16(0.11) |
| $^{133}$Cs | Set 1 | -19.88(0.03) | -0.87(0.36) |
| | Set 2 | -5.52(0.03) | -0.08(0.49) |
| | Set 3 | -15.10(0.02) | -0.62(0.22) |

**Table 6.3:** For all data sets the deviation between the measured and the calculated $\nu_z$ and $\nu_c^{conv}$ are listed. The magnitude of the deviation for the measured and the calculated axial frequency is larger than in the case of the conversion frequency. Comparing both deviations a correlation is visible.

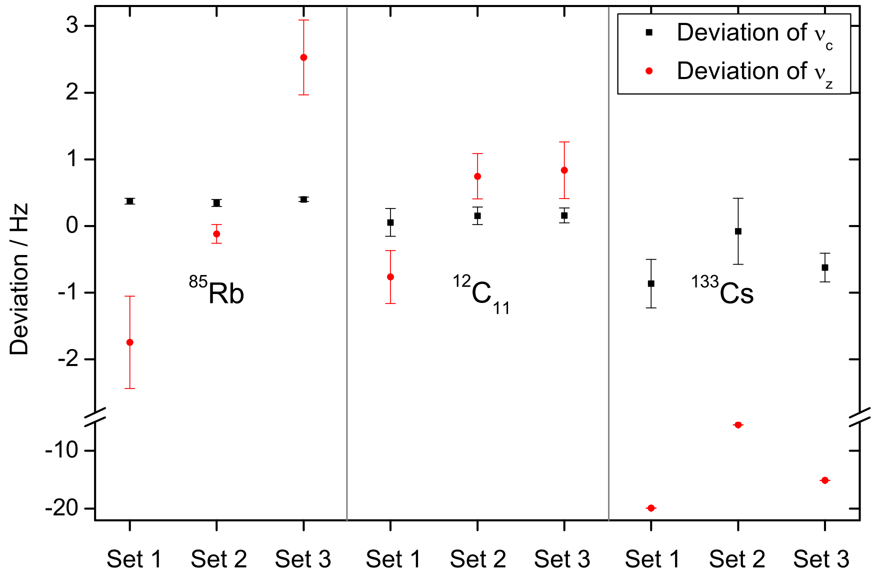

**Figure 6.7:** Deviation of the conversion frequency (black) and axial frequency (red) according to the values listed in Tab. 6.3.

### Magnetic field drift and fluctuations

A correlation between the temperature in the bore of the superconducting magnet and the conversion frequency and thus the magnetic field strength has been observed [MJ08]. During the measurement on $^{85}$Rb and $^{133}$Cs the temperature was recorded in the bore of the magnet close to the precision trap. A drift was observed as illustrated in Fig. 6.8. The effect of a change in temperature $\Delta T = 300$ mK on the conversion frequency $\nu_c^{conv}$ corresponds to $(\Delta\nu_c^{conv})_{temp,B} \approx 54$ mHz. A comparison of the conversion frequencies listed in Tab. 6.1 and the temperature drift shown in Fig. 6.8 confirms this shift quantitatively. The second effect caused by temperature changes is the change in the susceptibility of the material in the magnetic field. Therefore the magnetic field is disturbed, which is influencing the ion trajectories.

In the long term one has to consider the steady decrease in the magnetic field caused by a gradual decay of the current in the coils of the superconducting magnet. Each set of measurement took in the average 3 hours corresponding to fluctuations of the magnetic field strength of about $1.1 \cdot 10^{-8}$ T, resulting in fluctuations in $\nu_c^{conv}$ and $\nu_+$ of several mHz. Thus, this effect is comparable with the reached uncertainties in $\nu_c^{conv}$ and $\nu_+$. However, it is much smaller than the observed differences in $\Delta\nu_c$ for different ions, and can be therefore neglected.

### Changing trap dimensions

The temperature can affect the measured frequencies as well by influencing the trap dimensions due to material expansion. Since the trap is made of copper, which has an expansion coefficient of $\alpha = 16.5 \cdot 10^{-6}/K$, the dimensions of the trap are varying proportional to the temperature change. The effect on the radial eigenfrequencies is very small in comparison the to the change in the axial frequency. Considering the change of the trap parameter $d_0$ by $\Delta d_0$, the effect on the conversion frequency is negligible, whereas shifts in the eigenfrequencies are:

$$\begin{aligned} (\Delta\nu_\pm)_{temp,d} &\approx \frac{1}{2\pi}\frac{U_0}{B}\frac{\Delta d_0}{d_0^3} \\ &\text{and} \\ (\Delta\nu_z)_{temp,d} &\approx \frac{1}{2\pi}\sqrt{\frac{qU_0}{m}}\frac{\Delta d_0}{d_0^2}. \end{aligned} \tag{6.5}$$

Assuming $\Delta T = 300$ mK the corresponding frequency shifts for $^{133}$Cs are:

$$\begin{aligned} (\Delta\nu_\pm)_{temp,d} &\approx 11\,\text{mHz}, \\ (\Delta\nu_z)_{temp,d} &\approx 190\,\text{mHz}, \end{aligned}$$

which corresponds in both cases to a change in $\Delta\nu_c$ of a few mHz. Thus, it could explain part of the deviations of the frequency shifts within the measurements for each ion species.

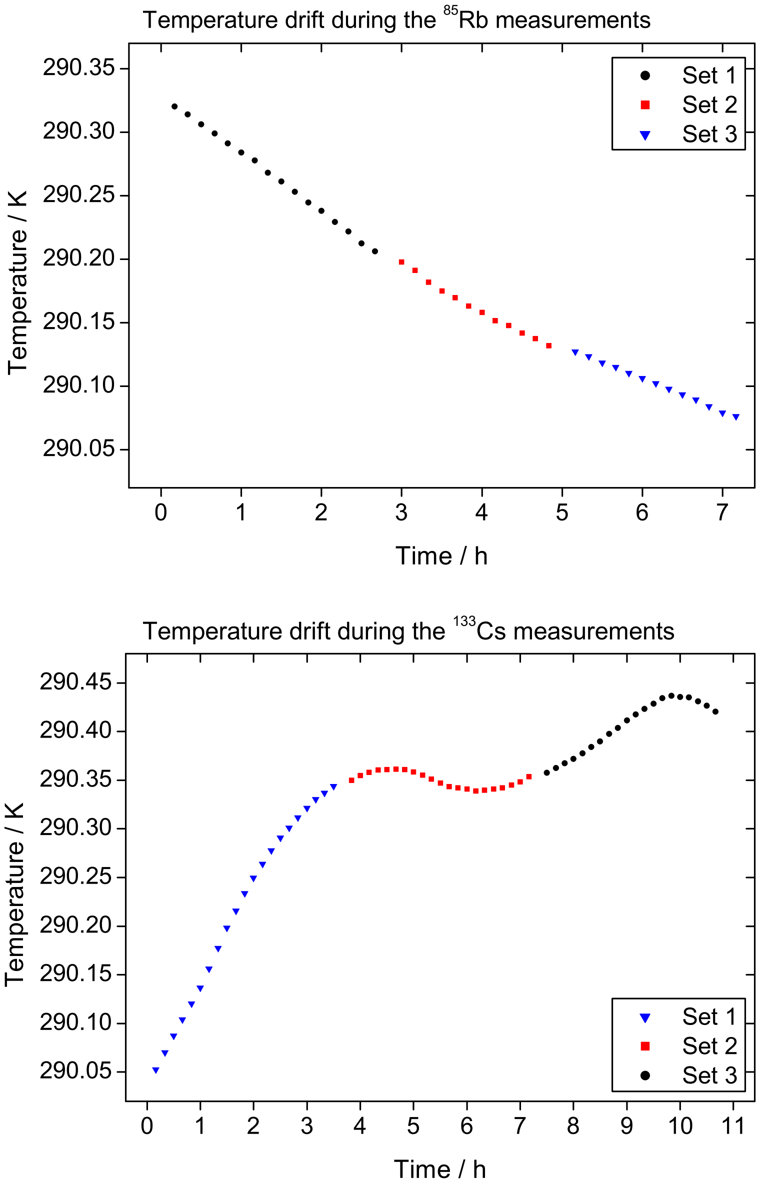

**Figure 6.8:** Temperature changes close to the precision trap, recorded during the measurements on $^{85}$Rb (top) and $^{133}$Cs (bottom). The duration of the measurement for one set corresponds to a temperature drift of $\Delta T_{min} \approx 20$ mK and $\Delta T_{max} \approx 300$ mK. Error bars are not presented since they are smaller than the symbol size.

### Voltage fluctuations

Recent measurements have shown that the voltages applied to the endcap and to the correction electrodes of the precision trap are not as stable as the voltage applied to the ring electrode. Since the endcap and the correction electrode potentials share the same AC(220V)-to-DC transformer, their fluctuations in time are correlated. An example for the voltages applied to the main electrodes is presented in Fig. 6.9. These data were recorded while no measurement cycle was running. Assuming similar voltage fluctuations during a measurement cycle the influence on the eigenfrequencies can be determined using the following relations:

$$\begin{aligned} (\delta\nu_z)_{volt} &= \frac{1}{2\pi}\cdot\sqrt{\frac{q}{md^2}}\cdot\left(\frac{\Delta U_0}{2\sqrt{U_0}}\right), && (6.6)\\ (\delta\nu_\pm)_{volt} &= \frac{1}{2\pi}\frac{1}{2Bd^2}\cdot\Delta U, && (6.7)\end{aligned}$$

with

$$\begin{aligned} (\delta\nu_z)_{volt} &\approx 6.8\,\mathrm{Hz}, && (6.8)\\ (\delta\nu_\pm)_{volt} &\approx 39\,\mathrm{mHz}, && (6.9)\end{aligned}$$

for $\delta U = 0.3$ mV. The effect on the conversion frequency $\nu_c^{conv}$ is negligible so that the normal measurements performed at ISOLTRAP are not affected by these fluctuations at the precision level routinely achieved. For the present measurement it has a strong influence on the axial frequency. To assure, that this is the reason for fluctuating axial frequencies, the frequency $\nu_z$ and the potential will be measured simultaneously in future measurements.

Another source of differences in $\Delta\nu_c$ is a different injection of the ions into the trap. This is connected to the fact, that to obtain the best transfer efficiency through the ISOLTRAP setup, the optimization of focusing and deflecting potentials has to be performed for each species individually, especially since there was a time gap of up to one month between the measurements of different ion species. A different injection leads to different ion trajectories in the trap, which in turn make the ions probe slightly different electric and magnetic fields. Connected to this are the amplitudes of the applied radiofrequencies, which depend on the excitation time (both parameters are presented in Tab. 6.4), and for the axial and the magnetron frequency also on other experimental conditions. This might lead to differences in the probed potential, and thus to differences in the resulting $\Delta\nu_c$.

### Discussion about the amplitude of the axial frequency $\nu_z$

The measurements of the axial frequency were performed with different excitation amplitudes and excitation times as shown in Tab. 6.4. For large amplitudes of the ion motion in axial direction the frequency is shifted because the quadrupolar potential is disturbed by an octupole term [Bro86]. The leading anharmonic correction can be expressed as:

$$\Delta U = \frac{1}{2}U_0\frac{C_4}{d^4}\left(z^4 - 3z^2\rho^2 + \frac{3}{8}\rho^4\right). \tag{6.10}$$

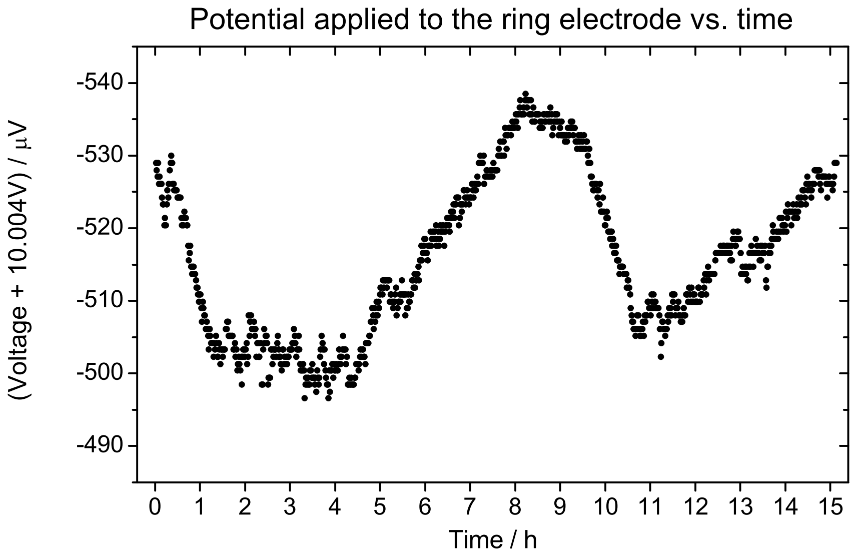

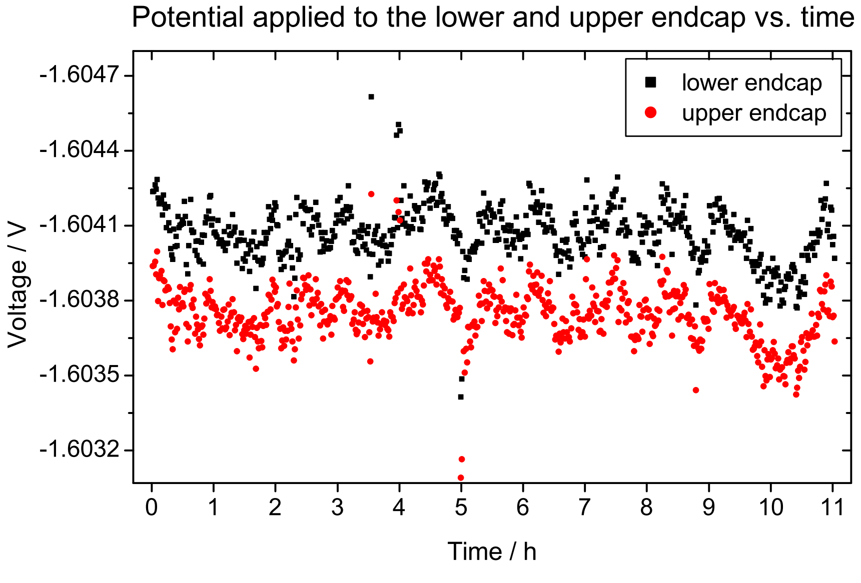

**Figure 6.9:** Fluctuations of the voltages applied to the main electrodes of the precision trap versus time. The potential of the ring electrode (top) shows a relative fluctuation of $\delta U/U \approx 3.4 \cdot 10^{-6}$ within 3 hours (corresponding to the duration of the measurement of one set). Below the voltages applied to the upper (red) and lower (black) endcap versus time are presented with a relative fluctuation of $\delta U/U \approx 2 \cdot 10^{-4}$ (during 3 hours). Error bars are not indicated since they are smaller than the symbol size.

| | | $^{85}$Rb | $^{12}$C$_{11}$ | $^{133}$Cs |
|---|---|---|---|---|
| $\nu_c$ | $a_{\mathrm{rf}}(\mathrm{V}_{pp})$ | 0.183 | 0.278 | 0.110 |
| | $T_{\mathrm{rf}}(\mathrm{s})$ | 1.2 | 0.9 | 2.0 |
| | $a_{\mathrm{rf}} \cdot T_{\mathrm{rf}}(\mathrm{Vs})$ | 0.220 | 0.250 | 0.220 |
| $\nu_+$ | $a_{\mathrm{rf}}(\mathrm{V}_{pp})$ | 0.002 | 0.038 | 0.002 |
| | $T_{\mathrm{rf}}(\mathrm{s})$ | 1.2 | 0.9 | 2.0 |
| | $a_{\mathrm{rf}} \cdot T_{\mathrm{rf}}(\mathrm{Vs})$ | 0.003 | 0.034 | 0.004 |
| $\nu_z$ | $a_{\mathrm{rf}}(\mathrm{V}_{pp})$ | 0.009 | 0.013 | 0.003 |
| | $T_{\mathrm{rf}}(\mathrm{s})$ | 0.1 | 0.1 | 0.4 |
| | $a_{\mathrm{rf}} \cdot T_{\mathrm{rf}}(\mathrm{Vs})$ | 0.001 | 0.001 | 0.001 |
| $\nu_-$ | $a_{\mathrm{rf}}(\mathrm{V}_{pp})$ | 0.008 | 0.070 | 0.010 |
| | $T_{\mathrm{rf}}(\mathrm{s})$ | 1.2 | 0.4 | 0.1 |
| | $a_{\mathrm{rf}} \cdot T_{\mathrm{rf}}(\mathrm{Vs})$ | 0.010 | 0.028 | 0.001 |

**Table 6.4:** Excitation times $T_{\mathrm{rf}}$ and rf amplitudes $a_{\mathrm{rf}}$ applied for the measurements of the conversion frequency and the eigenfrequencies. Within the measurement for each ion species these values were constant. Ideally the product of $T_{\mathrm{rf}}$ and $a_{\mathrm{rf}}$ should be constant to compare the results, which is not the case for the radial eigenfrequencies.

$C_4$ is constant for a certain set of voltages applied to the electrodes of the trap. Considering only the first term, since the coupling term ($\propto z^2\rho^2$) and the term for radial direction ($\propto \rho^4$) are very small, it leads to an axial frequency depending on the amplitude $a_z$ of the ion motion given by:

$$\nu_z'(a_z) = \left(1 - \frac{3}{4}C_4 \cdot \frac{a_z^2}{d^2}\right) \cdot \nu_z. \tag{6.11}$$

Assuming an amplitude of $a_z = 5\,\mathrm{mm}$ and $C_4 = -10^{-4}$ [Bec09] we obtain for $^{133}$Cs using Eq. (6.11) $\nu_z' - \nu_z =$-686 mHz. The value assumed for $C_4$ is based on simulations for the case that only correction tubes but no correction rings are implemented. Considering also the correction rings, the magnitude of $C_4$ and thus the magnitude of the deviation is expected to be even smaller [Bec09]. For a negative $C_4$ the trapping potential is lowered so that frequencies are determined too small (in comparison to the frequency in a harmonic trap). The amplitude $a_z$= 5 mm is an estimate and corresponds to an axial energy of $E_z$= 1 eV. An amplitude of $a_{z,max}$= 1 mm [Bec09] is assumed for the measurement of the conversion frequency. For the measurements of the axial frequency an axial dipole excitation scanned around $\nu_z$ was applied, therefore a higher amplitude is expected.

### Conclusion

The measurement of the conversion frequency and the three eigenfrequencies in a Penning trap were performed to determine the frequency shift $\Delta\nu_c$ between $\nu_c^{conv}$ and $\nu_c^{inv}$. Theoretically this shift is mass independent and provides information about trap imperfections, i.e. the ellipticity of the electrical field and the tilting angle of the magnetic field with respect to the symmetry axis of the trap.

Three different ion species were used for these studies and the average frequency shift for different masses is in the range of 100-350 mHz. Within the measurement for each nuclide the frequency shift for all three sets are comparable. The fact, that $\Delta\nu_c$ is different for different masses and ion species is based on many effects like different starting conditions, voltage fluctuations and different excitation amplitudes. The power supply providing the potential for the endcap and correction electrodes is not stable enough for the measurement of the eigenfrequencies but it does not effect the determination of the conversion frequency $\nu_c^{conv}$. The effects mentioned above are too large to eliminate the contribution due to trap imperfections out of the frequency shift $\Delta\nu_c$. Several test measurements have to be performed in order to find out whether the discrepancies are really based on the assumed reasons.

As soon as the starting conditions are optimized e.g. by using the temperature stabilization, exchanging the voltage source and investigating the sensitivity to rf amplitudes, the measurements will be repeated with better statistics. To improve the determination of the axial frequency another method can be used. Applying a dipolar excitation to the endcap electrodes (scanning $\nu_{\mathrm{rf}}$ around $\nu_z$) followed by a quadrupolar excitation with $\nu_{\mathrm{rf}}$ scanned around $\nu_+ - \nu_z$ to two segments of the endcap and the ring electrodes the coupling frequency allows to calculate the axial frequency. To determine the axial frequency one has to tune the dipolar axial frequency and the quadrupolar coupling frequency, which means that this measurement is more complicated in comparison to the procedure applied in the present studies. However, the ions have much less axial amplitude and stay in the harmonic field region. Additionally, the ellipticity can be determined by measuring the conversion frequency against the ellipticity, which is tunable externally [Bre08]. That allows to determine the present ellipticity. Therefore, the knowledge of the frequency shift and the ellipticity allow to calculate the tilting angle of the magnetic field with respect to the symmetry axis of the trap. This would lead to a characterization of the setup. Therefore one could correct for this shift in the evaluation of future mass measurements.

# Chapter 7

# Conclusion and Outlook

The present thesis reports on several activities at the online Penning trap mass spectrometer ISOLTRAP in order to study its systematic uncertainties using carbon cluster ions. The first one concerns an upgrade of the carbon-cluster laser ion source including several modifications and optimizations to the laser and ion optics. These were necessary to improve the mechanical stability and reliability, avoid discharges, and enhance the flexibility of the laser ion source with respect to the power density. The carbon-cluster laser ion source is advantageous for several reasons: At ISOLTRAP high-precision mass measurements are performed by determining the cyclotron frequency $\nu_c^{conv}$ of a charged particle in a Penning trap. For these measurements a magnetic field calibration with a reference ion of a well-known mass is very important. Carbon cluster ions are ideal for calibration purposes, as the atomic mass unit is defined as one twelfth of the mass of a $^{12}$C atom [Emi95]. The second advantage is that the masses provided by a carbon-cluster source are covering a large fraction of the nuclear chart. Therefore, the mass of the ion of interest is at maximum six mass units away from the mass of the reference ion, which minimizes the mass-dependent systematic uncertainty [Kel03]. Including the reported modifications the ion source was attached to the main ISOLTRAP beamline and a stable countrate in the order of a few up to tens carbon cluster ions was demonstrated depending on the laser power over several days. The optimization of the voltages applied to the electrodes of the ion source was performed such that the initial energy of the carbon cluster ions corresponds to the energy of the ions ejected from the buncher (i.e. ions from the surface ion source and ions provided by the ISOLDE beam). For the first time it is now possible to switch between the laser ion source and the ISOLDE beam, which is necessary to use the carbon cluster ions as reference ions for online experiments. Finally, the trapping of several cluster sizes was demonstrated in both, the preparation and the precision Penning trap so that time-of-flight spectra could be obtained for several cluster sizes $\mathrm{C}_n$ with $n \leq 25$.

For future measurements the ion transfer and the trapping in the preparation trap has to be improved to assure that for all cluster sizes $\mathrm{C}_n$ with $n \leq 25$ time-of-flight spectra can be recorded with the same efficiency. Especially the cooling procedure in the preparation trap has to be optimized.

As soon as the steps mentioned above are performed systematic studies using cross-reference measurements of carbon clusters are planned. Comparable studies have been performed in 2003 leading to the result of the mass-independent residual systematic uncertainty of $8 \cdot 10^{-9}$ [Kel03].
During this thesis work many beamtimes have been performed at ISOLTRAP. Over 20 masses were determined with relative mass uncertainties as low as $10^{-8}$, whereas many of them were measured for the first time. The masses of the nuclides addressed in 2008 are important input parameters for different fields of application, e.g. for the investigation of the proton-neutron interactions via $\delta V_{pn}$ values. For the first time, an isotope has been discovered at a Penning trap experiment: $^{229}$Rn. With the ISOLTRAP setup it was possible to measure the mass. The corresponding half-life was additionally determined using the tape station of the ISOLDE facility [Nei09].
As a further subject of this thesis tests of the systematic uncertainties using the invariance theorem were performed and corresponding measurements of the conversion frequency $\nu_c^{conv}$ and the three eigenfrequencies were accomplished for three different ion species ($^{85}$Rb, $^{12}$C$_{11}$, $^{133}$Cs). The measurement procedure leading to this frequency shift was described and sources of uncertainties were discussed. It was found that the measurement procedure is highly sensitive to several perturbations and starting conditions. Sources of uncertainties were identified and investigated so that future systematic studies will allow for a more precise determination of $\Delta\nu_c = \nu_c^{conv} - \nu_c^{inv}$.
While measuring the axial frequency $\nu_z$ over several hours, fluctuations of a few Hz have been observed. Since $\nu_z^2$ is proportional to the trapping potential, all voltages applied to the electrodes of the precision trap have been measured. It was observed that the power supply connected to the endcap and correction electrodes was fluctuating in the range of $\delta U/U = 10^{-4}$. This has no influence to the determination of the conversion frequencies $\nu_c^{conv}$, which is typically measured at ISOLTRAP, but in order to perform measurements of all eigenfrequencies a stable trapping potential is required. Therefore the power supply will be replaced. As a further source of systematic uncertainties temperature changes were observed. For technical reasons the temperature stabilization was not operating during the measurements. The temperature change of about 20 to 300 mK affects all measurements since it leads to a change of the magnetic field amplitude and influences the trapping parameter. For future measurements the developed and available temperature stabilization will be operated to reduce the temperature fluctuations down to a few 10 mK [MJ08].
The results of the frequency measurements allowed to calculate $\Delta\nu_c$, which was in the range of 100 to 350 mHz. Assuming realistic ellipticities and tilting angels of $\epsilon \leq 0.01$ and $\theta \leq 0.01$, respectively, the frequency deviation is expected to be in the range of 200 mHz. The knowledge of the frequency shift $\Delta\nu_c$ will allow for a more detailed knowledge on the trap parameters and might result in an improved systematic uncertainty at ISOLTRAP.
Adding an azimuthal quadrupolar electrostatic field to the trap potential, the conversion frequency $\nu_c^{conv}$ becomes a function of the ellipticity [Bre08]. Therefore, $\nu_c^{conv}(\epsilon)$ can be measured where the ellipticity can be varied external, which allows to calculate the ellipticity being present due to the misalignment of the trap electrodes. In combination with the studies presented above, the tilting angle $\theta$ can be calculated. The knowledge of the ellipticity and the tilting angle are important to characterize the trap, which might allow

for a correction of some of the systematic uncertainties. In the near future the measurements of the conversion and the eigenfrequencies will be repeated for different nuclides and carbon cluster ions with better defined and improved starting conditions.

# Bibliography

[Aud03] Audi, G. et al.: The AME2003 mass evaluation. In: *Nucl. Phys. A* 729 (2003), p. 129–336

[Bar08] Baruah, S. et al.: Mass measurements beyond the major r-process waiting point $^{80}$Zn. In: *Phys. Review Lett.* 101 (2008), p. 262501

[Bec93] Beck, D.: *Aufbau einer zylindrischen Penningfalle zum Einfang und Kühlen von Ionen*, Johannes Gutenberg-Universität Mainz, Diploma Thesis, 1993

[Bec09] Beck, D. et al.: Electric and magnetic field optimization procedure for Penning trap mass spectrometers. In: *Nucl. Inst. and Meth. A* 598 (2009), p. 635

[Bla02] Blaum, K. et al.: Carbon clusters for absolute mass measurements at ISOLTRAP. In: *Eur. Phys. J. A* 15 (2002), p. 245–248

[Bla03a] Blaum, K.: Recent developments at ISOLTRAP: towards a relative mass accuracy of exotic nuclei below $10^{-8}$. In: *J. Phys. B* 36 (2003), p. 921–930

[Bla03b] Blaum, K. et al.: Cluster calibration in mass spectrometry: laser desorption/ionization studies of atomic clusters and an application in precision mass spectrometry. In: *Anal. Bioanal. Chem.* 377 (2003), p. 1133–1139

[Bla04] Blaum, K.: Population inversion of nuclear states by a Penning trap mass spectrometer. In: *Eurphys. Lett.* 67(4) (2004), p. 586–592

[Bla05] Blaum, K. et al.: ISOLTRAP mass measurements of exotic nuclides at $\delta$m/m = $10^{-8}$. In: *Nucl. Phys. A* 752 (2005), p. 317c–320c

[Bla06] Blaum, K.: High-accuracy mass spectrometry with stored ions. In: *Phys. Rep.* 425 (2006), p. 1–78

[Bol92] Bollen, G. et al.: Resolution of nuclear ground and isomeric states by a Penning trap mass spectrometer. In: *Phys. Rev. Lett. C* 46 (1992), p. R2140–R2143

[Bre08] Breitenfeldt, M.: The elliptical Penning trap: Experimental investigations and simulations. In: *Int. J. of Mass Spec.* 275 (2008), p. 34–44

[Bro82] Brown, L. S. ; Gabrielse, G.: Precision spectroscopy of a charged particle in an imperfect Penning trap. In: *Physical Review A* 25 (1982), p. 2423

[Bro86] Brown, L. S.: Geonium theory: Physics of a single electron or ion in a Penning trap. In: *Rev. Mod. Phys.* 58 (1986), p. 243

[Deh90] Dehmelt, H.: Experiments with an isolated subatomic particle at rest. In: *Rev. Mod. Phys.* 62 (1990), p. 525

[Dyc04] Dyck, R. S. V.: Ultraprecise Atomic Mass Measurement of the $\alpha$ Particle and $^4$He. In: *Phys. Rev. Lett.* 22 (2004), p. 92

[Eid04] Eidelman, S. et al.: Review of Particle Physics. In: *Phys. Lett. B* 592 (2004), p. 1

[Emi95] Emiliani, C.: Redefinition of atomic mass unit, Avogadro constant, and mole. In: *Geochimica et Cosmochimica Acta* 59 (1995), p. 1205–1206

[Gab09] Gabrielse, G.: The true cyclotron frequency for particles and ions in a Penning trap. In: *Int. J. of Mass Spec.* 279 (2009), p. 107–112

[Gor08] Goriely, S. ; Pearson, J.M.: Further explorations of Skyrme-Hartree-Fock-Bogoliubov mass formulas. VIII. Role of Coulomb exchange. In: *Phys. Rev. C* 77 (2008), p. 031301(R)

[Grä80] Gräff, G. et al.: A Direct Determination of the Proton Electron Mass Ratio. In: *Z. Phys. A* 297 (1980), p. 35–39

[Gue07] Guenaut, C. et al.: High-precision mass measurements of nickel, copper, and gallium isotopes and the purported shell closure at $N = 40$. In: *Phys. Rev. C* 75 (2007), p. 044303

[Har08] Hardy, J. C. ; Towner, I. S.: Superallowed $0^+ \rightarrow 0^+$ nuclear $\beta$-decays: A new survey with precision tests of the conserved vector current hypothesis and the standard model. In: *Phys. Rev. C* 77 (2008), p. 025501

[Her01] Herfurth, F.: *A new ion beam cooler and buncher for ISOLTRAP and mass measurements of radioactive argon isotopes*, Rupertus Carola University of Heidelberg, Diss., 2001

[ISO03] `http://isolde.web.cern/ISOLDE/normal/separato.html`

[Kel03] Kellerbauer, A. et al.: From direct to absolute mass measurements: A study of the accuracy of ISOLTRAP. In: *Eur. Phys. J. D* 22 (2003), p. 53–64

[Kel04] Kellerbauer, A. et al.: Direct Mass Measurements on the Superallowed Emitter $^{74}$Rb and Its Daughter $^{74}$Kr: Isospin-Symmetry-Breaking Correction for Standard-Model Tests. In: *Phys. Rev. Lett.* 93 (2004), p. 072502–1

[Kön95a] König, M.: *Präzisionsmassenbestimmung instabiler Cäsium- und Bariumisotope in einer Penningfalle und Untersuchung der Ionenbewegung bei azimuthaler Quadrupolanregung*, Johannes Gutenberg-Universität Mainz, Diss., 1995

[Kön95b] König, M. et al.: Quadrupole excitation of stored ion motion at the true cyclotron frequency. In: *Int. J. of Mass Spec. and Ion Pr.* 142 (1995), p. 95–116

[Kös03] Köster, U. et al.: Resonant laser ionization of radioactive atoms. In: *Spec. Acta Part B* 58 (2003), p. 1047–1068

[Kug00] Kugler, E.: The ISOLDE facility. In: *Hyperfine interactions* 129 (2000), p. 23–42

[MJ08] Marie-Jeanne, M. et al.: Towards a magnetic field stabilization at ISOLTRAP for high-accuracy mass measurements on exotic nuclides. In: *Nucl. Inst. and Meth. in Phys. Res. A* 587 (2008), p. 464–473

[Muk04] Mukherjee, M.: *The mass of $^{22}$Mg and a concept for a novel laser ion source trap*, Ruperto-Carola Universität Heidelberg, Diss., 2004

[Muk08] Mukherjee, M. et al.: Mass measurements and evaluation around A = 22. In: *The Eur. Phys. J. A.* 35 (2008), p. 31–37

[Nei09] Neidherr, D. et al.: Discovery of $^{229}$Rn and the structure of the heaviest Rn and Ra isotopes from Penning-trap mass measurements. In: *Accepted for: Phys. Rev. Lett.* (2009)

[Rai04] Rainville, S. et al.: An ion balance for ultra-high-precision atomic mass measurements. In: *Science* 303 (2004), p. 334

[Red09] Redshaw, M. et al.: Penning-trap measurement of the atomic masses of $^{18}$O and $^{19}$F with uncertainties $<$0.1 parts per $10^9$. In: *Phys. Rev. A* 79 (2009), p. 012507

[Roo04] Roosbroeck, J. V. et al.: Unambiguous Identification of Three $\beta$-Decaying Isomers in $^{70}$Cu. In: *Phys. Rev. Lett.* 92 (2004), p. 112501

[Sav91] Savard, G. et al.: A new cooling technique for heavy ions in a Penning trap. In: *Phys. Lett. A* 158 (1991), p. 247–252

[Sch01] Schwarz, S. et al.: Accurate masses of neutron-deficient nuclides close to Z = 82. In: *Nucl. Phys. A* 693 (2001), p. 533–545

[Thi75] Thibault, C. et al.: Direct measurements of the masses of $^{11}$Li and $^{26,32}$Na with an on-line mass spectrometer. In: *Phys. Lett. C* 12 (1975), p. 644

[Web05] Weber, C. et al.: Weighing excited nuclear states with a Penning trap mass spectrometer. In: *Phys. Lett. A* 347 (2005), p. 81–87

[Wei06] Weinheimer, Ch.: Neutrino mass from triton decay. In: *Progress in Particle and Nuclear Physics* 57 (2006), p. 23–37

# Acknowledgements

At this point, I would like to thank the following people:

*Klaus Blaum* for his permanent care and advice, helpful discussions, not only about physics, and his support since 2007.

All ISOLTRAP members, especially: *Magdalena Kowalska*, *Dennis Neidherr* and *Martin Breitenfeldt* for their endless patience and support not only in the lab. *Christopher Borgmann*, *Alexander Herlert*, *David Lunney*, *Sarah Naimi*, *Marco Rosenbusch* and *Lutz Schweikhard* for their advice, for helping me preparing and performing the measurements and for the fun in the lab. Thank you for a great time at ISOLTRAP.

*Bruce Marsh* for his advice in laser physics. Thank you for borrowing the equipment, which was highly useful to prepare the measurements.

*Ermano Barbero* for his ideas concerning mechanics and materials but also for modifying parts of the cluster source.

*Ralf Zilly* and the workshop in Heidelberg at Max Planck Institute for Nuclear Physics for advice and machining parts of the cluster source.

All MATS members, especially *Szilard Nagy* and *Christian Smorra* for their advice concerning carbon cluster sources and *Stefan Ulmer* for many helpful discussions about the invariance theorem.

My friends for their encouragement during the whole time of my studies.

*Annette Lapp* for her corrections of this thesis.

My parents, *Karl* and *Irmgard* and my sister *Carina* for their backup during the whole time of my studies.

Last, but not least I would like to thank *Jürgen* for his endless support.